CONTRACT NAS8-30246

STUDY OF MULTIPLE HOLOGRAM RECORDING IN LITHIUM NIOBATE

T. K. Gaylord and W. R. Callen
School of Electrical Engineering
Georgia Institute of Technology
Atlanta, Georgia 30332

January 1976

FINAL REPORT PERIOD 1 OCTOBER 1973 – 1 JANUARY 1976

1976

Performed for

National Aeronautics and Space Administration
George C. Marshall Space Flight Center
Marshall Space Flight Center, Alabama 35812

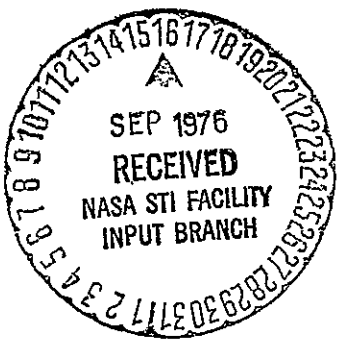

SCHOOL OF ELECTRICAL ENGINEERING
Georgia Institute of Technology
Atlanta, Georgia 30332

FINAL REPORT

PROJECT NO. E-21-633

STUDY OF MULTIPLE HOLOGRAM RECORDING IN LITHIUM NIOBATE

by

T. K. Gaylord and W. R. Callen

RESEARCH CONTRACT NAS8-30246

1 October 1973 to 1 January 1976

Performed for

NATIONAL AERONAUTICS AND SPACE ADMINISTRATION
George C. Marshall Space Flight Center
Marshall Space Flight Center, Alabama 35812

ABSTRACT

The results of a number of theoretical and experimental studies relating to multiple hologram recording in lithium niobate are reported. The analysis of holographic gratings stored in lithium niobate has been extended to cover a more realistic range of physical situations. A new successful dynamic (feedback) theory for describing recording, non-destructive reading, erasure, enhancement, and angular sensitivity has been developed. In addition, the possible architectures of mass data storage systems have been studied.

TABLE OF CONTENTS

I. INTRODUCTION

The possibility of high capacity, fast, random access storage by using three-dimensional optical holographic techniques has been known for more than five years now. This goal, however, has proved to be somewhat elusive and not as straightforward as originally anticipated. Full scale, full capability systems have not been built because of a number of problems. These problems are being investigated at Georgia Tech to determine 1) if fundamental, inherent limitations exist that were previously unknown and 2) what constitutes a sufficiently complete understanding of volume holography in ferroelectrics to allow routine engineering development of workable systems.

It is a pleasure to report that no inherent limiting factors have been found to date. This is of paramount importance. Indeed, the second aspect--that of developing a sufficient understanding of three dimensional holography has shown itself to be an area where additional basic scientific research is needed. Research is being pursued to provide this needed understanding. This final report covers this aspect of our work for the last nine months.

II. ANALYSIS OF HOLOGRAMS STORED IN LITHIUM NIOBATE

The description of the formation of phase holograms in ferroelectric crystals is strongly dependent on the internal electric field. Amodei has derived expressions [1] for the electric field patterns generated through diffusion and through drift respectively, for plane-wave holograms for the cases of the initial and the steady-state stages of holographic recording. We have greatly extended this model to cover the entire range of exposures in the formation of plane wave holograms. This is accomplished by a numerical approach, with both diffusion and drift of charge carriers included. The results of this approach reduce to the existing analytic expressions [1] for the electric field for the limiting cases of the initial and the final steady-state stages of hologram formation. Since analytic expressions for the electric field pattern, in general, cannot be obtained in the intermediate stages of holographic recording, the numerical approach permits the establishment of the limits of validity for the analytic expressions in terms of exposures and material parameters.

A corresponding problem is the determination of the refractive index profile of thick phase gratings in linear electro-optic crystals. In these materials, a sinusoidal light intensity pattern does not necessarily produce a sinusoidal change in the index of refraction or a change that is in phase with the recording intensity pattern. Depending on the crystals, the details of exposure, and the physical mechanisms in the process of hologram recording, different grating

profiles and different spatial phase shifts may be generated. Therefore, in the study of microscopic physical processes in these optically-induced phase gratings, a knowledge of the resulting gratings is of fundamental importance.

We have developed a method for determining the grating profile of thick gratings in linear electro-optic crystals. This method also determines the effective photovoltaic field and the relative contributions of diffusion and drift during hologram recording. The method requires only a knowledge of the modulation ratio during hologram recording and the fundamental and the higher-order diffraction efficiencies of the grating. Thus, simple external measurements reveal the microscopic internal properties.

Complete details of the work on the formation of phase holograms in ferroelectric crystals and on the determination of refractive index profile and physical processes can be found in References [2], [3], and [4], which are reproduced here for completeness.

Unified approach to the formation of phase holograms in ferroelectric crystals*

S. F. Su and T. K. Gaylord

School of Electrical Engineering, Georgia Institute of Technology, Atlanta, Georgia 30332
(Received 16 June 1975; in final form 2 September 1975)

The description of the formation of thick-phase holograms over the entire range of exposures has been accomplished using numerical methods. The internal electric field distributions (and thus the refractive-index profiles for linear electro-optic crystals) generated through diffusion and through drift of charge carriers are calculated. The treatment allows for the presence of an effective electric field due to the photovoltaic effect and an externally applied electric field. The results of this approach reduce to the existing analytic expressions for the limiting cases of the initial and the steady-state stages of hologram formation. This approach establishes the limits of validity for the analytic expressions in terms of exposure and material parameters.

PACS numbers: 42 30.N, 42.40 K, 78 20 J

I. INTRODUCTION

The recording of thick-phase holograms in ferroelectric crystals was first shown in lithium niobate by Chen *et al.*[1] The grating patterns of the holograms were optically induced refractive-index changes in the bulk material. Their work stimulated study of the theory of hologram formation in ferroelectrics. Three different models of the physical mechanisms have been proposed[2–4] to explain the phenomenon of this optically induced refractive-index change. Chen[2] explained the refractive-index change by drift of photoexcited carriers under the influence of an internal electric field. He assumed that there are electron traps in the material. Initially, some of the traps are filled (neutral charge state) and they provide electrons upon photoexcitation. The others are empty and they capture electrons. In addition, he assumed that there is an internal electric field in the direction opposite to that of the spontaneous polarization. The photoexcited electrons drift toward the positive side of the field (or the spontaneous polarization) leaving behind positive charges of ionized trap centers. The photoexcited charges will be retrapped and reexcited out of the traps until they finally drift out of the illuminated region and are trapped. Therefore, a space-charge field is created between the positive ionized centers and the trapped negative charges. This space-charge field causes the spatial variation of the refractive index via the linear electro-optic effect of the sample. The need for an internal field in Chen's model was removed by Glass *et al.*[5] by introducing the concept of a high-field photoeffect. They found that the current inside the crystal is due to a bulk photovoltaic effect and not due to internal fields.

Johnston[3] proposed a light-generated polarization pattern to explain the variation of the refractive index. In his model, an extremely high density of free electrons are required to generate the large field necessary to account for the variation of the refractive index.

Another model has been proposed by Amodei.[4] He has pointed out that charge migration by diffusion is an important factor in holographic recording for sufficiently small grating periods. He has shown that even in the absence of an internal field or an externally applied field, the photoexcited electrons still can migrate out of the illuminated region by thermal processes. Further, he has derived[6] expressions for the electric field patterns generated through diffusion and through drift, respectively, for plane-wave holograms for the cases of the initial and the steady-state stages of holographic recording.

Young *et al.*[7] have generalized Amodei's formulation by removing the assumption that the diffusion length is small compared to a grating period. This treatment applies only to the initial stage of hologram formation.

In this paper, Amodei's model is extended to cover the entire range of exposures in the formation of plane-wave holograms. This is accomplished by a numerical approach and both the diffusion and the drift of charge carriers are included. The electric field distributions generated through these two mechanisms are obtained. The results of this approach reduce to the existing analytic expressions[6] for the limiting cases of the initial and the final steady-state stages of hologram formation. Since analytic expressions for the electric field pattern, in general, cannot be obtained in the intermediate stages of holographic recording, the numerical approach permits the establishment of the limits of validity for the analytic expressions in terms of exposures and material parameters.

II. THEORY

Two plane waves of wavelength λ having angles of incidence upon the medium of $+\theta$ and $-\theta$ produce an interference pattern inside the medium of intensity $I(x)=I_0(1+m\cos Kx)$, where I_0 is the sum of the intensities (power per unit area transverse to the direction of energy flow) of the two waves, m is the modulation ratio $(0<m\leq 1)$, x is the direction perpendicular to the bisector of the angle between the beams, and $K=2\pi/L$, where $L=\lambda/2\sin\theta$. Staebler and Amodei[8] have shown for lithium niobate that the electric field patterns, which cause the spatial variation of the refractive index, are generated through both diffusion and drift of photogenerated free electrons (as opposed to holes). Thus the charge carriers will be assumed to be electrons. The method is equally applicable to holes, however. Assuming that the concentration of trapped electrons is sufficiently large so that its variation due to migration

is negligibly small and that the generation rate and trapping time are essentially unchanged during recording, then the concentration of free electrons excited to the conduction band is given by[6]

$$n(x)=\tau g_0(1+m\cos Kx), \tag{1}$$

where τ is the lifetime of charge carriers and g_0, the generation rate, is given by[6]

$$g_0=I_0\alpha/hf, \tag{2}$$

where α is the optical absorption coefficient, h is Planck's constant, and f is the light frequency. For an isotropic material (or if the x direction is along one of the crystallographic axes for an anisotropic material), the spatial distribution of the current density at any time is given by

$$J(x,t)=eD_n\frac{dn}{dx}+e\mu_n n[E_0'+E_{sc}(x,t)]+\kappa_1\alpha I, \tag{3}$$

where e is the magnitude of the electronic charge, D_n is the diffusion coefficient for electrons, μ_n is the mobility for electrons, E_0' is the externally applied field (if any), $E_{sc}(x,t)$ is the space-charge field, and κ_1 is a constant depending on the nature of the absorption center and wavelength.[5] The third term on the right-hand side of Eq. (3) represents the photovoltaic effect.[5] Using Eq. (1) and the definition of I, Eq. (3) can be rewritten as

$$J(x,t)=eD_n\frac{dn}{dx}+e\mu_n n[E_0+E_{sc}(x,t)], \tag{4}$$

where

$$E_0\equiv E_0'+\frac{\kappa_1\alpha I_0}{e\mu_n\tau g_0}. \tag{5}$$

The last term in Eq. (5) may be regarded as an effective field due to the photovoltaic effect. Using the Einstein relation, $\mu_n/D_n=e/kT$, where k is the Boltzmann constant and T is the absolute temperature, the current density, Eq. (4), can be rewritten as

$$J(x,t)=e\mu_n\left(\frac{kT}{e}\frac{dn}{dx}+n[E_0+E_{sc}(x,t)]\right). \tag{6}$$

The accumulation rate of the space-charge density ρ at any point and at any time is given by the one-dimensional continuity equation,

$$\frac{\partial\rho(x,t)}{\partial t}=-\frac{\partial J(x,t)}{\partial x}. \tag{7}$$

Combining this with Poisson's equation gives

$$\frac{\partial E_{sc}(x,t)}{\partial x}=\frac{\rho(x,t)}{\epsilon}=-\frac{1}{\epsilon}\int_0^t\frac{\partial J(x,t')}{\partial x}\,dt', \tag{8}$$

where ϵ is the permittivity of the material. Equation (8) cannot be solved analytically except in the limiting case of the initial stage of hologram formation in which $E_{sc}(x,t)$ is neglected in the transport equation. Therefore, a numerical approach was employed to reveal the behavior of $E_{sc}(x,t)$ for the exposures in which $E_{sc}(x,t)$ cannot be neglected in the transport equation. The total space-charge field is $E_{sc}(x,t)\equiv E_{sc}'(x,t)+E_{sc}''(x,t)$, where $E_{sc}'(x,t)$ and $E_{sc}''(x,t)$ are the space-charge fields due to diffusion and drift, respectively. In order to obtain a better insight into the relative importance of diffusion and drift, these two mechanisms are considered separately as follows.

A. Diffusion only (no internal or externally applied field)

In this case, $E_0=0$ and $E_{sc}(x,t)=E_{sc}'(x,t)$, therefore Eq. (6) becomes

$$J(x,t)=e\mu_n\tau g_0\times[-(kT/e)mK\sin Kx+(1+m\cos Kx)E_{sc}'(x,t)]. \tag{9}$$

The exposure time t is set equal to $p\Delta t$, where p is any positive integer and Δt is a constant increment of the exposure time that is sufficiently small so that the variation of dJ/dx is negligible over the time interval Δt. Then, Eq. (8) reduces to a difference-differential equation,

$$\frac{dE_{sc}(x,p\Delta t)}{dx}=\frac{dE_{sc}(x,(p-1)\Delta t)}{dx}-\frac{1}{\epsilon}\frac{dJ(x,(p-1)\Delta t)}{dx}\Delta t. \tag{10}$$

Substituting Eq. (9) into Eq. (10) with E_{sc} replaced by E_{sc}', we obtain

$$\frac{dE_{sc}'(x,p\Delta t)}{dx}=\frac{dE_{sc}'(x,(p-1)\Delta t)}{dx}+\left(\frac{e\mu_n\tau g_0}{\epsilon}\right)\times\left[\left(\frac{kT}{e}\right)mK^2\cos Kx-(1+m\cos Kx)\times\frac{dE_{sc}'(x,(p-1)\Delta t)}{dx}+mK\sin(Kx)\times E_{sc}'(x,(p-1)\Delta t)\right]\Delta t. \tag{11}$$

From Eq. (11), together with the boundary condition $E_{sc}'(0,t)=0$ and the initial condition $\partial E_{sc}'(x,0)/\partial x=0$, the space-charge field, $E_{sc}'(x,t)$, can be obtained by numerical integration.

B. Drift only (with large dc field)

In this case, there is a dc field that is sufficiently large so that the diffusion component of the current can be neglected compared with the drift component. Therefore, Eq. (6) becomes

$$J(x,t)=e\mu_n\tau g_0(1+m\cos Kx)[E_0+E_{sc}''(x,t)]. \tag{12}$$

Letting the exposure time t be equal to $p\Delta t$ and substituting Eq. (12) into Eq. (10) with E_{sc} replaced by E_{sc}'' gives

$$\frac{dE_{sc}''(x,p\Delta t)}{dx}=\frac{dE_{sc}''(x,(p-1)\Delta t)}{dx}+\left(\frac{e\mu_n\tau g_0}{\epsilon}\right)\times\left(mK\sin(Kx)[E_0+E_{sc}''(x,(p-1)\Delta t)]-(1+m\cos Kx)\frac{dE_{sc}''(x,(p-1)\Delta t)}{dx}\right)\Delta t. \tag{13}$$

Equation (13) is the difference-differential equation for drift. It can also be solved numerically for E_0+E_{sc}'', provided that the boundary and the initial conditions are specified.

C. Diffusion and drift

When the electric field, E_0 (externally applied field plus effective photovoltaic field), is small such that

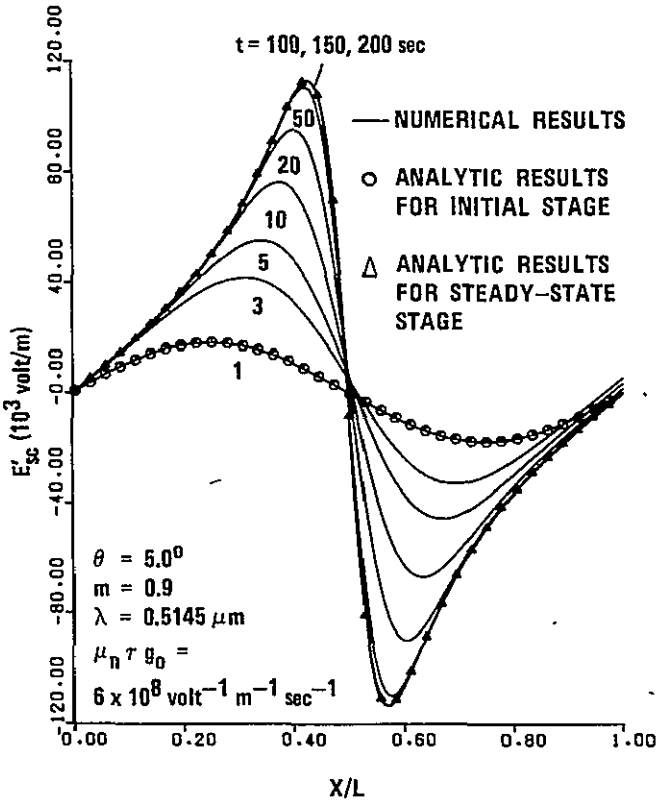

FIG. 1. One grating period of the calculated space-charge field, $E'_{sc}(x,t)$, produced by diffusion.

both the diffusion and drift components are present, the space-charge field is the superposition of the fields due to these two components. That is, $E_{sc}=E'_{sc}+E''_{sc}$. Usually, when the electric field E_0 is several hundred thousand volts per meter, the space-charge field due to diffusion is very small compared with the space-charge field due to drift.

III. RESULTS AND DISCUSSION

Equations (11) and (13) were numerically solved by use of the Runge-Kutta method. As can be seen from these equations the controlling material parameter is $\mu_n\tau g_0/\epsilon$. The low-frequency permittivity ϵ is known for most ferroelectrics as a function of temperature and crystallographic direction. For lithium niobate at room temperature, a typical value is $\epsilon=30\epsilon_0$, where ϵ_0 is the permittivity of free space. Values for the parameters μ_n and τ are not accurately known. Photoconductivity data for doped lithium niobate[5] imply that the product $\mu_n\tau\approx10^{-13}$ m^2/V (using $e\mu_n\tau\alpha/hf=1.4\times10^{-10}$ m/V^2 and $\alpha=3.8\times10^3$ m^{-1} from Ref. 5). The generation rate g_0 can vary over an extremely wide range depending on the doping and treatment of the sample as well as the intensity of the laser beams. A typical value of $g_0=6\times10^{22}$ m^{-3} sec^{-1} is chosen here and thus $\mu_n\tau g_0=6\times10^8$ V^{-1} m^{-1} sec^{-1} in this work. The exposure time increment Δt was 1 sec. The space-charge field distribution for diffusion is shown in Fig. 1. Figure 1 shows that for the initial stage of hologram formation (after a 1-sec exposure time in this case), the field distribution is sinusoidal. As the exposure increases, the amplitude of the space-charge field increases and the field distribution becomes nonsinusoidal, and the positions at which the field extrema occur are shifted. However, the field pattern retains odd symmetry at all stages of hologram formation. When the steady-state stage of hologram formation is reached (after about a 100-sec exposure), the amplitude and the distribution of the space-charge field pattern remain fixed and do not change with further exposure. For comparison, the results of the analytic solutions for the initial and the final steady-state stages of hologram formation are also shown in Fig. 1. The circles in Fig. 1 represent the results for the initial stage of hologram formation as obtained from the analytic expression[6]

$$E'_{sc}(x,t)=(1/\epsilon)kT\mu_n\tau g_0 mKt\sin Kx, \tag{14}$$

evaluated for an exposure time of 1 sec with $\mu_n\tau g_0=6\times10^8$ V^{-1} m^{-1} sec^{-1}. The triangles in Fig. 1 represent the results for the steady-state stage of hologram formation as obtained from the analytic expression[6]

$$E'_{sc}(x)=(kT/e)(mK\sin Kx)(1+m\cos Kx)^{-1}, \tag{15}$$

evaluated at room temperature. The comparison shows that the numerical results correctly reduce to the analytic results for the limiting cases. In addition, the limits of validity for Eqs. (14) and (15) are established by the numerical approach in terms of exposure and material parameters. For example, from Fig. 1, it is seen that Eq. (14) is valid when $t\leq1$ sec and that Eq. (15) is valid when t is near or greater than 100 sec for the parameters used here. Figure 2 presents the behavior of the amplitude of the space-charge field as a function of exposure. The amplitude increases rapidly in the early stages of hologram formation. For $\mu_n\tau g_0$

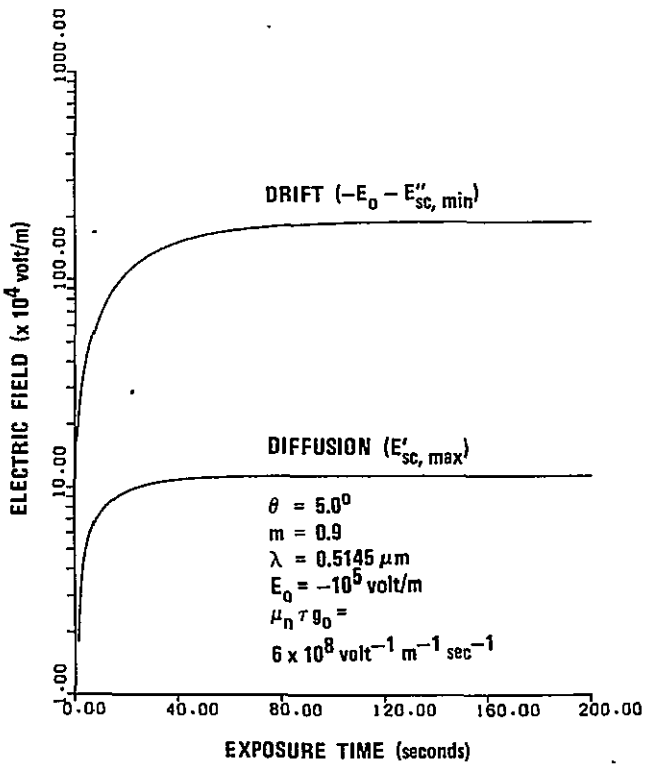

FIG. 2. Calculated values of the space-charge field amplitude produced by diffusion and by drift as a function of exposure time.

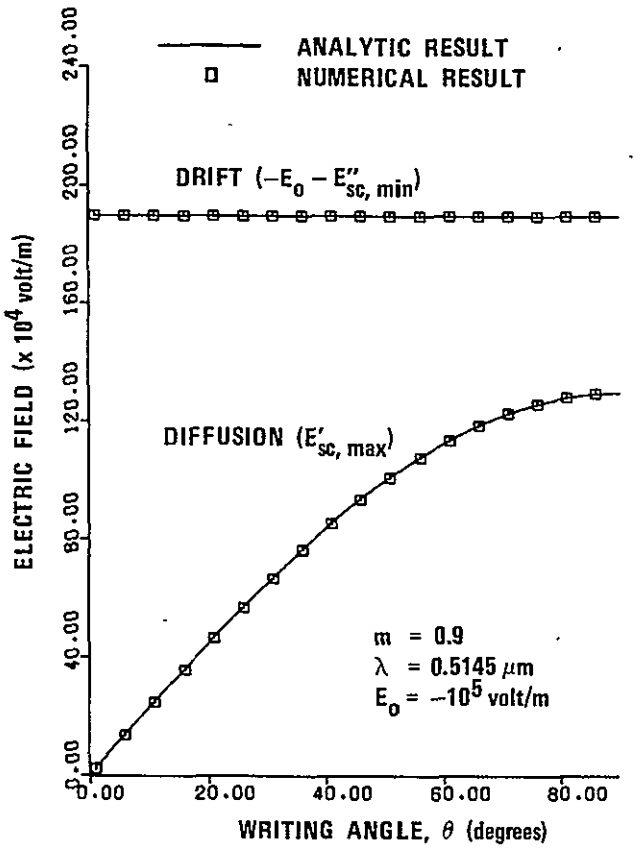

FIG. 3. Calculated steady-state final amplitude of the space-charge field produced by diffusion and by drift as a function of writing angle.

$= 6\times10^8\ V^{-1}\,m^{-1}\,sec^{-1}$, the amplitude begins to saturate near 40 sec of exposure and finally remains unchanged after about 100 sec of exposure. Since the value of g_0 is proportional to I_0 as given by Eq. (2), the limits of validity of Eqs. (14) and (15) depend on I_0 for a given set of material parameters. Larger values of I_0 result in larger values of g_0 and, therefore, shorter exposure times are needed to reach any given exposure. In other words, the amplitude of the field saturates more rapidly for larger values of g_0. Equation (14), for the case of the initial stage of hologram formation, is valid as long as the space-charge field is negligible in the transport equation. Strictly speaking, the space-charge field cannot be neglected at any time except at the very beginning of hologram formation. In the numerical approach, the space-charge field is neglected in the transport equation only for an exposure time of Δt in duration from the beginning of hologram formation. In the calculation of the results here, Δt was chosen to be 1 sec. In fact, other values of Δt can be used, provided that the values of Δt are small enough to assure that there is no appreciable variation in dJ/dx over the time interval Δt. In addition to $\Delta t = 1.0$ sec, the calculations have been performed with $\Delta t = 0.5$ sec and the same resultant electric field patterns are obtained. In general, in order to maintain the same level of numerical accuracy, a smaller value of Δt must be used for a larger value of g_0 for given material parameters, writing angle, and beam modulation ratio.

Figure 3 presents the amplitude of the space-charge field as a function of writing angle in the steady-state stage of hologram formation. The squares in Fig. 3 represent the numerical results, while the solid curve represents the analytic solution. The field amplitude for diffusion increases as writing angle increases (grating period decreases). This is true for all stages of hologram formation though only the steady-state case is shown in Fig. 3. The space-charge field amplitude as a function of the modulation ratio m for the steady-state case is shown in Fig. 4. Again, the results of the numerical method and the analytic solution are represented by the squares and the solid curve, respectively. The field amplitude increases as the modulation ratio increases. This is also true for all other stages of hologram formation.

In the case of drift, the electric field at the boundary is not zero. It depends on the charge density at the surface and the applied voltage across the sample. The electric field at the boundary is assumed to be equal to the dc field E_0 at all times. The shape of the electric field pattern produced is independent of the value of the dc field E_0. The amplitude of the pattern, however, is dependent upon E_0, increasing with increasing E_0. The initial condition for drift is $\partial E''_{sc}(x, 0)/\partial x = 0$. Figure 5 shows the total electric field distribution when drift is dominant. The dc field E_0 is assumed to be -1.0×10^5 V/m. As for the diffusion case, the field distribution is sinusoidal at the initial stage of hologram formation. As exposure increases, the amplitude increases and the field distribution becomes nonsinusoidal and sharply

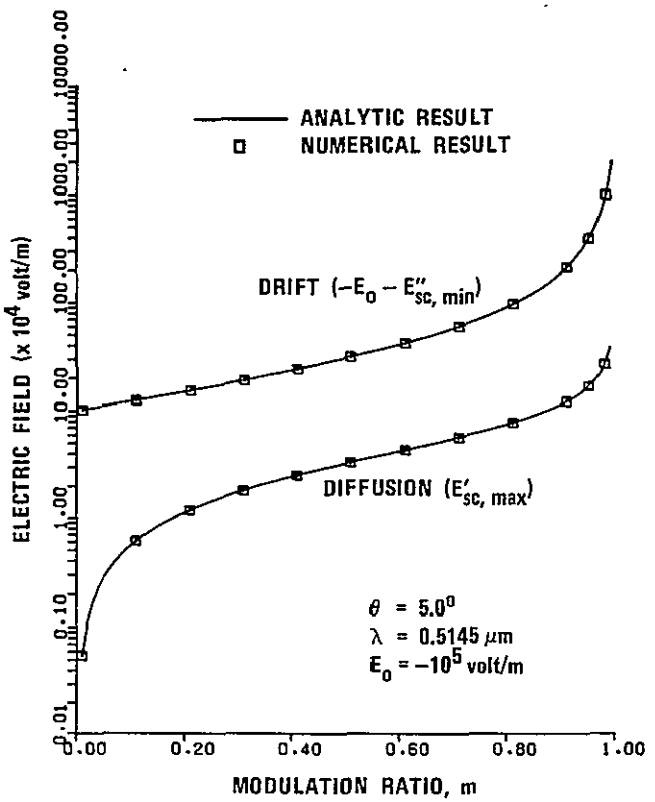

FIG. 4. Calculated steady-state final amplitude of the space-charge field produced by diffusion and by drift as a function of beam modulation ratio.

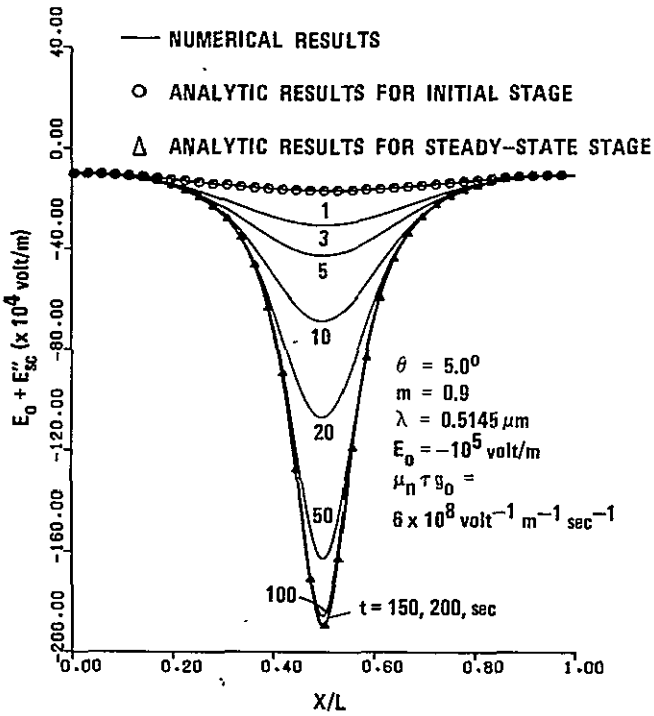

FIG. 5. One grating period of the calculated total electric field, $E(x,t)=E_0+E''_{sc}(x,t)$, produced by drift.

peaked. However, the positions at which the field extrema occur do not shift with exposure. In addition, the field pattern has even symmetry at all times. Also shown in Fig. 5 are the analytic solutions for the electric field distribution at the initial and the steady-state stages of hologram formation. The same value for the electric field at the boundary has been used in these analytic solutions. The circles in Fig. 5 represent the results of the initial stage solution (proportional to $\cos Kx$). The triangles represent the steady-state solution [proportional to $(1+m)/(1+m\cos Kx)$]. The numerical results again correctly reduce to the analytic solutions in these limiting cases of the initial and the steady-state stages of hologram formation. From Fig. 5, it is observed that, for $\mu_n\tau g_0=6\times10^8\ \mathrm{V^{-1}\,m^{-1}\,sec^{-1}}$, the analytic solutions are valid when t is equal to or less than 1 sec for the initial stage of hologram recording and when t is near or greater than 150 sec for the steady-state case. The behavior of the drift electric field amplitude as a function of exposure is also plotted in Fig. 2. The saturation time is about 150 sec for $\mu_n\tau g_0=6\times10^8\ \mathrm{V^{-1}\,m^{-1}\,sec^{-1}}$, which is somewhat longer than that for the diffusion case. Figure 3 contains the steady-state drift electric field amplitude as a function of writing angle. It is observed that the amplitude does not change with the writing angle (and therefore grating period). This is also true for all other stages of hologram formation as well. In Fig. 4, the steady-state drift electric field amplitude as a function of the beam modulation ratio is plotted. It shows that only when the beam modulation ratio is greater than about 0.8 will an appreciable amplitude of the electric field be produced.

These results indicate the following distinctions between the electric field pattern produced by the diffusion mechanism and that produced by the drift mechanism:

(i) The electric field pattern due to diffusion has odd symmetry at all times, whereas the field pattern due to drift has even symmetry at all times.

(ii) For diffusion, the field amplitude increases as writing angle increases (decreasing grating period). For drift, the field amplitude is independent of the writing angle (and grating period).

(iii) The exposure time needed to reach steady state is somewhat longer for drift than for diffusion. In other words, the field due to diffusion saturates more rapidly than the field due to drift.

(iv) In the case of diffusion, the position for the maximum (and minimum) value of the electric field is a function of exposure. In the case of drift, the position for the field maximum (and minimum) remains fixed for all exposures.

(v) There is a 90.0° phase difference between the fundamental Fourier component of the electric field patterns for diffusion and drift for all exposures.

The analysis of this paper is applicable if holes instead of electrons were the charge carriers. For the case of hole charge carriers, the electric field pattern due to diffusion is the same as that produced by electrons except that it is reflected about the $x=0$ axis [$E'_{sc}(x,t)$ becomes $E'_{sc}(-x,t)$]. The electric field patterns due to drift are independent of the type of charge carriers.

The electric field (due to diffusion and/or drift) in ferroelectric lithium niobate causes a spatial modulation of the refractive index via the electro-optic effect. For lithium niobate, the electro-optic effect is linear (Pockels effect). Thus, the amplitude of the modulation of the refractive index is proportional to the magnitude of the electric field. Therefore, the refractive-index pattern caused by the electric field via the electro-optic effect is the same as the electric field pattern calculated here. It follows that the spatial distribution of the refractive index (grating shape) resulting from diffusion is different from that resulting from drift. Since different grating shapes produce different distributions of the higher-order diffraction efficiencies,[9] these higher-order diffraction efficiencies of a hologram grating produced by diffusion are different from those of a hologram grating produced by drift. This indicates the possibility that the physical mechanisms (diffusion and/or drift) that occur during the hologram formation may be determined by measuring the higher-order diffraction efficiencies of a hologram.

IV. CONCLUSIONS

The internal electric field patterns generated by diffusion and drift during hologram recording in ferroelectric crystals were obtained by numerically solving the appropriate difference-differential equations. Unlike previous analytic solutions, this method is applicable for all exposure times. These numerical results reduce to existing analytic results for the limiting cases of the initial and the final steady-state stages of hologram formation. For a given set of material parameters, the

limits of validity of the analytic solutions as well as further distinctions between diffusion and drift have been revealed.

Note added in proof. Calculations of the internal electric field distributions for all stages of hologram development have recently been made using analytical methods. A closed-form solution has been presented by G.A. Alphonse, R.C. Alig, D.L. Staebler, and W. Phillips [RCA Rev. 36, 213 (1975)] using the assumption that their function G is equal to $e\mu_n \tau g_0 E_0/\epsilon$. Analytical results have also been obtained assuming $E_{sc}(0, t) = 0$ (as in the present work) by W.D. Cornish, M.G. Moharam, and L. Young (unpublished).

*Work supported by the National Science Foundation and by the National Aeronautics and Space Administration.

[1]F.S. Chen, J. T. LaMacchia, and D.B. Fraser, Appl. Phys. Lett. 13, 223 (1968).
[2]F.S. Chen, J. Appl. Phys. 40, 3389 (1969).
[3]W.D. Johnston, Jr., J. Appl. Phys. 41, 3279 (1970).
[4]J.J. Amodei, Appl. Phys. Lett. 18, 22 (1971).
[5]A.M. Glass, D. von der Linde, and T.J. Negran, Appl. Phys. Lett. 25, 233 (1974).
[6]J.J. Amodei, RCA Rev. 32, 185 (1971).
[7]L. Young, W.K.Y. Wong, M.L. W. Thewalt, and W.D. Cornish, Appl. Phys. Lett. 24, 264 (1974).
[8]D.L. Staebler and J.J. Amodei, J. Appl. Phys. 43, 1042 (1972).
[9]S.F. Su and T.K. Gaylord, J. Opt. Soc. Am. 65, 59 (1975).

Determination of physical parameters and processes in hologram formation in ferroelectrics*

S. F. Su and T. K. Gaylord

School of Electrical Engineering, Georgia Institute of Technology, Atlanta, Georgia 30332
(Received 29 January 1976)

The material parameters and physical processes during hologram formation in ferroelectric crystals have previously been identified. Some methods (based largely on new diagnostic techniques) for evaluating these critical parameters and for quantifying the physical processes are summarized here.

PACS numbers. 42.40.Kw, 42 30.Nt, 78.20 Jq

A multitude of applications exist for volume (thick) holograms and gratings. The use of ferroelectric crystals such as lithium niobate for volume holographic recording was established by Chen, LaMacchia, and Fraser.[1] Since then there has been considerable experimentation and analysis involving these materials. The holographic diffraction efficiency has been shown to be very sensitive to the material parameters and the physical processes that are operative in these linear electro-optic materials. The physical processes, in turn, are largely dependent on the recording conditions. Some methods for evaluating the material parameters and quantifying the physical processes are summarized here.

The physical processes occurring during hologram recording are known to be diffusion and drift of electrons.[2,3] The resultant space-charge electric field modulates the index of refraction via the linear electro-optic effect. There may be an effective electric field due to the bulk photovoltaic effect[4] and/or an externally applied electric field during recording. A charge transport analysis[2,5–7] of the holographic recording process in these electro-optic crystals indicates that the controlling parameter is $e\mu_n\tau g_0 t/\epsilon$, where e is the magnitude of the electronic charge, μ_n is the electron mobility, τ is the electron lifetime, g_0 is the electron photogeneration rate, t is the exposure time, and ϵ is the low-frequency dielectric permittivity. The permittivity (a tensor) is well known for any given direction in most crystals. The exposure time t is externally controlled and is thus known. The unknown (and highly variable) factor is therefore $\mu_n\tau g_0$.

The product $\mu_n\tau g_0$ may be calculated via several methods. One method is by evaluation of the exposure parameter u. The exposure parameter, which is defined as $u\equiv\mu_n\tau g_0 t$, may be evaluated from a knowledge of the beam modulation ratio m during recording, the measured fundamental diffraction efficiency DE_1, and the higher-order diffraction efficiencies, DE_2, DE_3, etc. A detailed procedure for determining u is given in Ref. 8. Since the exposure duration t is known, the product $\mu_n\tau g_0$ is then determined by u/t. A second method to obtain the product $\mu_n\tau g_0$ is via a single-beam erasure experiment. The normal decay of the diffraction efficiency η of any hologram from its initial value η_0 under uniform illumination can be shown[5] to be

$$\sin^{-1}(\eta^{1/2})/\sin^{-1}(\eta_0^{1/2})=\exp(-e\mu_n\tau g_0 t/\epsilon). \quad (1)$$

From measurements of η and η_0, the product $\mu_n\tau g_0$ may be obtained for known t. For small diffraction efficiencies, Eq. (1) reduces to $\eta=\eta_0\exp(-2e\mu_n\tau g_0 t/\epsilon)$ as given in Ref. 5. A third method to evaluate $\mu_n\tau g_0$ is by measurement of the photoconductivity σ, since $\sigma=e\mu_n n=e\mu_n\tau g_0$, where n is the photogenerated electron concentration.

The photogeneration rate g_0 is proportional to the total intensity I_0 and the optical absorption coefficient α of the crystal. It is given by $g_0=\alpha I_0/hf$, where h is Planck's constant and f is the optical frequency. Thus, g_0 may be determined from I_0, α, and f. It is difficult to evaluate μ_n and τ separately. The product $\mu_n\tau$ is frequently treated as a single parameter. If g_0 has been obtained, the product $\mu_n\tau$ may be determined using any one of the three methods mentioned previously.

The physical processes of diffusion and drift during hologram recording are conveniently quantified by giving the effective diffusion electric field E_D and the effective internal drift electric field E_0. The field E_D is given by $(kT/e)K$, where k is Boltzmann's constant, T is the absolute temperature during recording, and $K=2\pi/L$, where L is the grating period. The field E_0 is the sum of an effective bulk photovoltaic field and the applied field (if any). The relative magnitudes of the effective fields are a measure of the relative contributions of diffusion and drift. Thus,

$$\%\ \text{diffusion}=[E_D/(E_D+|E_0|)]\times 100\%, \quad (2)$$

and

$$\%\ \text{drift}=[E_0/(E_D+|E_0|)]\times 100\%. \quad (3)$$

Usually K and T are known and, therefore, E_D can be easily calculated.

The value of E_0 may be evaluated several ways. From a knowledge of the beam modulation ratio during recording and the measured fundamental and higher-order diffraction efficiencies, the field E_0 can be determined.[8] The procedure involves first determining the exposure parameter u and then determining the Fourier components of the refractive-index profile. These Fourier components determine the grating profile. By a best fit of the analytical expression for the space-charge field, which is a function of u and E_0, to the grating profile, the value of E_0 may be determined.

The value of E_0 may also be evaluated via photocurrent measurements. It has been shown[4] that the effective photovoltaic electric field is given by

$$E_0 = \kappa_1 hf / e\mu_n \tau, \quad (4)$$

where κ_1 is a constant that is proportional to the induced photocurrent and is dependent on the impurity centers involved. For example, for iron-doped lithium niobate, Glass *et al.*[4] have found a value of κ_1 to be about 3.0×10^{-11} A m/W. From Eq. (4), E_0 may be evaluated from a knowledge of κ_1, f, and the product $\mu_n \tau$.

A third method for determining E_0 is by direct experimentation. The magnitude of an externally applied electric field (along the c axis) may be varied until the electric field is found that produces the minimum writing sensitivity. In this situation, it is assumed that the external electric field is cancelling the effective internal field E_0, and thus E_0 is equal in magnitude and opposite in direction to the applied field that yields minium sensitivity.

For small exposures which produce sinusoidal or nearly sinusoidal refractive index gratings, the physical processes of diffusion and drift may be quantified by evaluating the parameter ϕ_n, which is the spatial phase difference between the hologram-forming light interference pattern and the resulting refractive-index profile. The range of values for ϕ_n is from 0° (pure drift) to 90° (pure diffusion).[3] For a light interference pattern with a maximum at the coordinate system origin, diffusion contributes sine grating components and drift contributes cosine grating components. The value of the parameter ϕ_n is determined by the relative amplitudes of the fundamental sine grating and the fundamental cosine grating. Specifically, $\phi_n = |\tan^{-1}(n_{s_1}/n_{c_1})|$, where n_{s_1} and n_{c_1} are the fundamental sine and cosine components, respectively. These two quantities may be determined from m, DE_1, DE_2, etc.[8] Therefore, ϕ_n may also be quantified.

For illustration, a hologram was recorded in a 2.12-mm-thick 0.02-mole% iron-doped lithium-niobate crystal possessing an absorption coefficient of 0.37 m^{-1}. The hologram was written with a wavelength of 514.5 nm, a total intensity of 8.77 mW/mm^2, external angles of incidence of $\pm 5.00°$, a recording time of 187 sec, polarization in the plane of incidence, a modulation ratio of 0.994, and no applied electric field. For this case, it was determined by the methods summarized in this letter that $u = 4.74 \times 10^8$ $V^{-1} m^{-1}$ (using $\epsilon = 30\epsilon_0$, where ϵ_0 is the permittivity for free space), $g_0 = 8.39 \times 10^{21}$ $m^{-3} sec^{-1}$, $\mu_n \tau = 3.04 \times 10^{-16}$ V^{-1} m^2, $E_D = 5.50 \times 10^4$ V m^{-1}, $E_0 = -1.06 \times 10^5$ V m^{-1}, $\phi_n = 27.3°$, % diffusion = 34%, and % drift = 66%. An external electric field during recording applied in the $+c$ or $-c$ directions was found, respectively, to subtract or to add to E_0. This changes the relative contributions of diffusion and drift. In addition, the diffraction efficiencies, the Fourier grating components, and ϕ_n also are changed by the application of an electric field during recording.

*Work supported by the National Science Foundation and by the National Aeronautics and Space Administration.

[1]F.S. Chen, J.T. LaMacchia, and D.B. Fraser, Appl. Phys. Lett. 13, 223 (1968).
[2]J.J. Amodei, RCA Rev. 32, 185 (1971).
[3]D.L. Staebler and J.J. Amodei, J. Appl. Phys. 43, 1042 (1972).
[4]A.M. Glass, D. von der Linde, and T.J. Negran, Appl. Phys. Lett. 25, 233 (1974).
[5]G.A. Alphonse, R.C. Alig, D.L. Staebler, and W. Phillips, RCA Rev. 36, 213 (1975).
[6]W.D. Cornish, M.G. Moharam, and L. Young, J. Appl. Phys. (to be published).
[7]S.F. Su and T.K. Gaylord, J. Appl. Phys. 46, 5208 (1975).
[8]S.F. Su and T.K. Gaylord, Appl. Opt. (to be published).

Applied Optics, vol. 15, no. 8, August 1976.

Refractive-Index Profile and Physical Process Determination in Thick Gratings in Electro-Optic Crystals*

S. F. Su and T. K. Gaylord

A method for determining the refractive index profile of thick phase gratings in linear electro-optic crystals is presented. This method also determines the effective photovoltaic electric field and the relative contributions of diffusion and drift during hologram recording. The method requires only a knowledge of the modulation ratio during hologram recording and the fundamental and the higher-order diffraction efficiencies of the grating. As an illustration of the method, the refractive index profile, the effective photovoltaic field, and the relative contributions of diffusion and drift are determined from experimental measurements for a lithium niobate holographic grating.

The authors are with the School of Electrical Engineering, Georgia Institute of Technology, Atlanta, Georgia 30332.

Received 28 February 1976.

I. Introduction

Volume (thick) holographic gratings have numerous applications. They can be used as highly efficient diffraction gratings, narrow band spectral filters, thick grating optical components such as lenses, imaging systems capable of spectral resolution of extended objects, and as a variety of components in integrated optics. The materials used for recording volume holograms, in general, exhibit light-induced changes in refractive index (photorefractive effect) or changes in optical absorption or both. Photorefractive materials include linear electro-optic crystals such as lithium niobate. In these materials, a sinusoidal light intensity pattern does not necessarily produce a sinusoidal change in the index of refraction or a change that is in phase with the recording intensity pattern. Depending on the crystals, the details of exposure, and the physical mechanisms in the process of hologram recording, different grating profiles and different spatial phase shifts may be generated.[1-4] Therefore, in the study of microscopic physical processes in these optically-induced phase gratings, a knowledge of the resultant gratings is of fundamental importance.

In this paper, a method for determining the grating profile of thick gratings in linear electro-optic crystals is presented. This method also determines the effective photovoltaic field and the relative contributions of diffusion and drift during hologram recording. The method requires only a knowledge of the modulation ratio during hologram recording and the fundamental and the higher-order diffraction efficiencies of the grating. Thus, simple external measurements reveal the microscopic internal properties.

To test the calculational accuracy of the method, the refractive index profiles of thick gratings are determined from the calculated diffraction efficiency data for some known grating profiles. Comparison of the determined profiles to the original profiles verifies that the method is very accurate. Further, as an illustration of the method, the refractive index profile, the

effective photovoltaic field, and the relative contributions of diffusion and drift are determined from experimental measurements for a lithium niobate holographic grating.

II. The Model

The geometry used for a thick optically-induced grating is presented in Fig. 1. The +x direction is chosen to coincide with the +c axis direction of the crystal and is in the plane of incidence and parallel to the surfaces of the crystal, the y axis is perpendicular to the page, and the z axis is perpendicular to the surfaces of the crystal. The crystal is assumed to be lossless and the grating is assumed to be pure phase grating. The light intensity producing the grating is the sinusoidal interference pattern produced by the intersection of two plane waves and is given by

$$I(x) = I_o (1 + M \cos Kx), \tag{1}$$

where I_o is the sum of the intensities of the two waves, $K = 2\pi/L$, L is the grating period given by $L = \lambda/2\sin\theta$, λ is the free space wavelength of the writing beams, θ is the angle of incidence, and M is the modulation ratio. The physical processes through which the grating is generated are known to be diffusion and drift of photoexcited electrons.[5] Also, an externally applied electric field and/or an effective photovoltaic field[6] may exist during the process of hologram recording. The grating profile inside the crystal is periodic (but not necessarily sinusoidal) in the x direction. For simplicity, the grating is assumed to be uniform in the z direction.

III. Determination of the Refractive Index Profile

A. Theoretical Analysis

The space-charge electric field patterns, and therefore the grating profiles, generated through diffusion and drift of electrons can be obtained for any given wavelength, exposure, material parameters, and geometrical

configuration either by analytical methods,[2,3] or by numerical methods.[4] An analytical expression for the space-charge field patterns can be shown to be

$$E_{sc}(x,t) = [(kT/e)\,MK \sin Kx + M E_o (1 - \cos Kx)]\,(1 + M \cos Kx)^{-1}$$
$$\times \{1 - \exp[(-e\mu_n \tau g_o t/\epsilon)(1 + M \cos Kx)]\}, \qquad (2)$$

where k is Boltzmann's constant, T is the absolute temperature, e is the magnitude of the electronic charge, μ_n is the electron mobility, τ is the lifetime of the photoexcited electrons, g_o is the electron photo-generation rate, t is the exposure time, ϵ is the permittivity of the crystal, and E_o is the effective electric field during hologram recording, which is the sum of the effective photovoltaic field and an externally applied field (if any). When multiplied by an appropriate electro-optic coefficient, Eq. (2) becomes a general expression for the grating profiles. The term containing sin Kx in Eq. (2) is due to diffusion and the term containing (1 - cos Kx) is due to drift. From Eq. (2), it is seen that, for a given wavelength and geometrical configuration in holographic recording, the controlling parameters are E_o and $\mu_n \tau g_o t/\epsilon$. The permittivity (a tensor) is well known for any given direction in most crystals. The exposure time t is externally controlled and is thus also known. Without accurate measurements of the material parameters in advance, the values of E_o and $\mu_n \tau g_o$ are usually not known during the process of holographic recording. Therefore, with E_o and $\mu_n \tau g_o$ unknown, Eq. (2) does not represent any particular grating profile but a family of grating profiles. However, Eq. (2) contains information about the allowed profiles. From Eq. (2), it is seen that the grating profiles generated through diffusion of electrons have odd symmetry with respect to x = 0 (intensity maximum during recording) and can be represented by a sine series. Likewise, the grating profiles generated through drift have even symmetry with respect to x = 0 and can be represented by a cosine series. The refractive index modulation amplitude,

which is proportional to $E_{sc}(x)$ at any time, is periodic and can be written as a Fourier series

$$\Delta n(x) \equiv n(x) - n_o = \sum_{h=1}^{\infty} [n_{sh} \sin(hKx) + n_{ch} \cos(hKx)], \tag{3}$$

where $n(x)$ is the grating refractive index profile, n_o is the average value of $n(x)$, and n_{sh} and n_{ch} are the amplitudes of higher-order harmonic gratings due to diffusion and drift, respectively. The subscripts s, c, and h denote the quantities associated with the sine gratings, the cosine gratings, and the h th-harmonic grating, respectively. By use of Eq. (2), it can easily be shown that the higher-order harmonic gratings, n_{sh} and n_{ch}, can be expressed in terms of their corresponding fundamental gratings as

$$n_{sh} = n_{s1} f_{sh} = n_{s1} \int_0^{2\pi} g_1(v) \sin(hv)\, dv \Big/ \int_0^{2\pi} g_1(v) \sin v\, dv, \tag{4}$$

and

$$n_{ch} = n_{c1} f_{ch} = n_{c1} \int_0^{2\pi} g_2(v) \cos(hv)\, dv \Big/ \int_0^{2\pi} g_2(v) \cos v\, dv, \tag{5}$$

where

$$g_1(v) = \sin v\,(1 + M \cos v)^{-1}\{1 - \exp[(-eu/\epsilon)(1 + M \cos v)]\}, \tag{6}$$

and

$$g_2(v) = (1 - \cos v)(1 + M \cos v)^{-1}\{1 - \exp[(-eu/\epsilon)(1 + M \cos v)]\}, \tag{7}$$

where $u \equiv \mu_n \tau g_o t$ and $v \equiv Kx$. From Eqs. (4) through (7), it is observed that f_{sh} and f_{ch} are independent of E_o and K. They are functions of M and u only. That is, for a given value of M, $f_{sh} = f_{sh}(u)$ and $f_{ch} = f_{ch}(u)$. Using this property and the expression for diffraction efficiency,[7] the grating profile of a thick grating can be determined.

B. The Method

By the method of Ref. 7, the m th-order diffraction efficiency for an E mode incident wave (wave polarized in plane of incident) of free space wavelength λ' at the m th-order Bragg angle θ_m can be shown to be

$$DE_m = \sin^2\left\{\left[\left[\sum_h^m \left(\frac{L^{(m_h-1)}}{(m_h-1)!\,(h)^{(m_h-1)}}\right)^2 \left(\frac{\{[(n_{sh})^2 + (n_{ch})^2]^{\frac{1}{2}}\}^{m_h}}{(\lambda')^{(2m_h-1)}}\right)\right.\right.$$

$$\times (n_o)^{(m_h-1)} \cos[m_h \tan^{-1}(n_{sh}/n_{ch})]\Big]^2 + \left[\sum_h^m \left(\frac{L^{(m_h-1)}}{(m_h-1)!\,(h)^{(m_h-1)}}\right)^2\right.$$

$$\times \left(\frac{\{[(n_{sh})^2 + (n_{ch})^2]^{\frac{1}{2}}\}^{m_h}}{(\lambda')^{(2m_h-1)}}\right) (n_o)^{(m_h-1)} \sin[m_h \tan^{-1}(n_{sh}/n_{ch})]\Big]^2\Big]^{\frac{1}{2}}$$

$$\left.\left. \times \frac{\pi d \cos(2\theta_m)}{\cos\varphi_m}\right)\right., \qquad (8)$$

where φ_m is the refraction angle given by $\varphi_m = \sin^{-1}[(\sin\theta_m)/n_o]$ and m_h is an integer representing the m_h th mode (with respect to the h th-harmonic grating) excited due to the h th-harmonic grating. The symbol $\sum_h^m$ denotes the summation over all of the values of h that divide evenly into the integer m. A detailed discussion of the relationships among the integers m, h, and m_h is given in Ref. 7 for both exact Bragg conditions and nearly exact Bragg conditions. The quantities n_o, λ', θ_m, and DE_m (m = 1, 2, 3, $\cdots$) are now given and the Fourier components n_{sh} and n_{ch} (h = 1, 2, 3, $\cdots$) are the quantities to be determined. The grating period, if not given, can be obtained by $L = \lambda'/2\sin\theta_1$.

From Eq. (8), the first- and second-order diffraction efficiencies are

$$DE_1 = \sin^2\{[(n_{s1})^2 + (n_{c1})^2]^{\frac{1}{2}} \pi d \cos(2\theta_1)/(\lambda' \cos\varphi_1)\}, \qquad (9)$$

and

$$DE_2 = \sin^2\left[\left(\left\{L^2 n_o[(n_{c1})^2 - (n_{s1})^2]/(\lambda')^2 + n_{c2}\right\}^2 + [2L^2 n_o n_{s1} n_{c1} /(\lambda')^2 + n_{s2}]^2\right)^{\frac{1}{2}} \pi d \cos(2\theta_2)/(\lambda' \cos\varphi_2)\right]. \quad (10)$$

Substituting Eqs. (4) and (5) into Eq. (10) with h = 2 gives

$$DE_2 = \sin^2\left[\left(\left\{L^2 n_o[(n_{c1})^2 - (n_{s1})^2]/(\lambda')^2 + n_{c1} f_{c2}\right\}^2 + [2L^2 n_o n_{s1} n_{c1} /(\lambda')^2 + n_{s1} f_{s2}]^2\right)^{\frac{1}{2}} \pi d \cos(2\theta_2)/(\lambda' \cos\varphi_2)\right]. \quad (11)$$

Since the values of f_{s2} and f_{c2} can be calculated for any given value of u via Eqs. (4) and (5), n_{s1} and n_{c1} can be obtained for the same value of u by solving Eqs. (9) and (11) simultaneously. Thus, solving Eqs. (9) and (11) using a particular value of u, say u_1, we get a pair of solutions denoted by $n_{s1}(u_1)$ and $n_{c1}(u_1)$. The signs of $n_{s1}(u_1)$ and $n_{c1}(u_1)$ must be carefully chosen.[8,9] Once $n_{s1}(u_1)$ and $n_{c1}(u_1)$ are obtained, the corresponding higher-order Fourier components, $n_{sh}(u_1)$ and $n_{ch}(u_1)$, h = 2, 3, ···, can be obtained by Eqs. (4) and (5). With this set of Fourier components, the corresponding set of higher-order diffraction efficiencies $[DE_m(u_1)$, m = 3,4, ···] are calculated. This entire process [starting from solving Eqs. (9) and (11)] is then repeated for other values of u. Using numerical techniques, a search is made for the particular u, say u_p, that gives the calculated higher-order diffraction efficiencies best matching the initially given values. The corresponding Fourier components $n_{sh}(u_p)$ and $n_{ch}(u_p)$, h = 1, 2, 3, ···, are the solutions desired, and the refractive index profile is obtained by inserting $n_{sh}(u_p)$ and $n_{ch}(u_p)$ into Eq. (3).

C. Calculational Accuracy of the Method

The method was numerically implemented and tested by determining the

Fourier components of three typical gratings from the calculated diffraction efficiencies [using Eq. (8)] of these gratings. The first few orders of the Fourier components of the refractive index profile of these gratings are listed in the "original" rows in Table I. The diffraction efficiencies of these gratings are calculated with $\lambda' = 514.5$ nm. With these diffraction efficiency data, the Fourier components of the refractive index profile of the gratings are then determined using the foregoing method. The Fourier components determined are listed in the "calculated" rows in Table I. From Table I, it is seen that the method yields excellent numerical accuracy. Other reading wavelengths ($\lambda' = 488.0$ nm and $\lambda' = 632.8$ nm) have also been used to perform these calculations and similar results were obtained. This shows that the reading wavelength λ' used in the method does not necessarily have to be equal to the writing wavelength λ and that the refractive index profile determined is independent of the reading wavelength.

D. Effect of Diffraction Efficiency Errors

In practice, the diffraction efficiencies are measured values, and therefore, some experimental error is unavoidable. These experimental errors will affect the refractive index profile determined by the method. However, if the errors are small, a reasonably accurate grating profile can still be obtained. This is illustrated in Fig. 2. The central curve in Fig. 2 represents the actual profile of a grating. The other curves in Fig. 2 represent the grating profiles determined from diffraction efficiencies which are 5% higher and 5% lower than those corresponding to the actual profile. From Fig. 2, it is observed that a several percent systematic error in the diffraction efficiencies results in a small change in the grating profile determined by the method. In addition to the grating profile presented in Fig. 2, other grating profiles produced with smaller exposure parameters have also been

analyzed. It is found that the error in the grating profile decreases with decreasing exposure parameters. If, instead of a systematic error, a random error of the same standard deviation is present, the determined profile similarly approximates the actual profile.

E. Effect of Boundary Reflections

The effect of boundary reflections was not included in the foregoing analysis. To include this, the measured diffraction efficiency at each Bragg angle must be corrected by dividing by the appropriate transmittance factor τ_m. When the surfaces of the grating are perfectly flat and perfectly parallel, this transmittance factor for the m th-order diffraction is given by[10]

$$\tau_m = (1 - R_m)^2[1 + 2R_m\cos(2\beta_m d) + (R_m)^2]/\{[1 - (R_m)^2]^2 + 4(R_m)^2 \times [\cos^2(2\nu_m d) + \cos^2(2\beta_m d)] - 4R_m[1 + (R_m)^2]\cos(2\nu_m d)\cos(2\beta_m d)\}, \quad (12)$$

where $R_m = \tan^2(\theta_m - \varphi_m)/\tan^2(\theta_m + \varphi_m)$, $\beta_m = 2\pi n_o(\cos\varphi_m)/\lambda'$, and $\nu_m d$ is the argument of the sine squared function in Eq. (8). In most practical cases, the surfaces of the grating are neither perfectly flat nor perfectly parallel. If the cosine factors in Eq. (12) average to zero due to variations in thickness over the illuminated region, the transmittance factor reduces to $\tau_m = (1 - R_m)^2/[1 + (R_m)^2]$.

IV. Determination of Effective Photovoltaic Field and Physical Processes

It has been shown in the preceding section that the refractive index profile of a grating in a linear electro-optic crystal can be determined by knowing the modulation ratio during hologram recording and the fundamental and the higher-order diffraction efficiencies of the grating. The information from Eq. (2) used in determining the grating profile was independent of the effective electric field E_o. Therefore, the value of E_o can be obtained by

a best fit of Eq. (2) to the grating profile determined by the method in the preceding section. The effective photovoltaic field can thus be obtained by subtracting the externally applied field (if any) from E_o.

The physical processes of diffusion and drift during hologram recording are conveniently quantified by the effective diffusion electric field E_D, which is given by $(kT/e)K$, and the effective electric field E_o. The relative magnitudes of the effective fields are a measure of the relative contributions of diffusion and drift. Thus,

$$(\% \text{ diffusion}) = [E_D/(E_D + |E_o|)] \times 100\%, \tag{13}$$

and

$$(\% \text{ drift}) = [|E_o|/(E_D + |E_o|)] \times 100\%. \tag{14}$$

V. Experimental Results

For illustration, the refractive index profile of a lithium niobate holographic grating is determined from measurements of its fundamental and higher-order diffraction efficiencies. The holographic grating was recorded in a 2.12-mm-thick 0.02-mole% Fe-doped lithium niobate crystal with the grating vector parallel to the c axis of the crystal. The hologram was written with a wavelength of 514.5 nm, a total power density of 8.77 mW/mm^2, external writing angles of $\pm 5.00^\circ$, a writing time of 187 sec, polarization in the plane of incidence, a modulation ratio of 0.994, and no externally applied field. The diffraction efficiencies were measured with a low power He-Ne laser ($\lambda' = 632.8$ nm) The measured diffraction efficiencies were $DE_1 = 21.6\%$, $DE_2 = 8.64 \times 10^{-2}\%$, and $DE_3 = 7.74 \times 10^{-3}\%$. When corrected by their corresponding transmittance factors, the diffraction efficiencies became $DE_1 = 29.7\%$, $DE_2 = 0.123\%$, and $DE_3 = 1.08 \times 10^{-2}\%$. These corrected diffraction efficiencies were then used in the method to determine the refractive index profile of the grating. The

exposure parameter for this grating was found to be $u_p = 4.74 \times 10^8$ $V^{-1}m^{-1}$ for $\epsilon = 30\,\epsilon_o$, where ϵ_o is the permittivity for free space. The resultant refractive index profile is shown in Fig. 3. This particular grating profile is nearly sinusoidal due to the relatively small exposure. By fitting Eq. (2) to the profile in Fig. 3, it was found that the effective electric field during hologram recording was $E_o = -1.06 \times 10^5$ V/m (in -c direction). This value is larger than the values reported by Cornish et al.[2] but smaller than the values reported by Glass et al.[6] The value of E_D was found to be 5.5×10^4 V/m. Thus, (% diffusion) = 34% and (% drift) = 66% for this particular grating.

For small exposures which produce sinusoidal or nearly sinusoidal refractive index gratings, the physical processes of diffusion and drift may be quantified by evaluating the parameter ϕ_n, which is the spatial phase difference between the hologram-forming light interference pattern and the resulting refractive index profile. The range of values for ϕ_n is from 0° (pure drift) to 90° (pure diffusion).[5] For a light interference pattern with a maximum at the coordinate system origin, diffusion contributes sine grating components and drift contributes cosine grating components. The value of the parameter ϕ_n is determined by the relative amplitudes of the fundamental sine grating and the fundamental cosine grating. Specifically, $\phi_n = |\tan^{-1}(n_{s1}/n_{c1})|$, where n_{s1} and n_{c1} are the fundamental sine and cosine components, respectively. For this experimental case it was found that $\phi_n = 27.3^\circ$.

Determinations of the grating profile and physical processes have also been performed for gratings recorded in an applied electric field. An external field during recording applied in the +c or -c axis directions of the crystal was found respectively to decrease or to increase E_o and thus to decrease or to increase the relative contribution of drift. The relative drift contribution has been experimentally altered by an external field from essentially 0% to nearly 100%.

VI. Discussion

Because the incident angle of the reading beam can not exceed 90.0°, the number of higher-order Bragg angles available is limited to the integer that is nearest to, but less than $2L/\lambda'$. If a suitably short wavelength source is available, the accessibility of higher-order Bragg angles is assured. However, the higher-order diffraction efficiencies are often small and thus the first three or so orders of the diffraction efficiency are usually sufficient.

The method presented in this paper can also be applied to the case in which the reading beam is polarized perpendicular to the plane of incidence (H mode). It can be shown straightforwardly that the grating profiles determined are independent of the polarization of the reading beam.

The phenomenon of birefringence must, in principle, also be taken into account. Here, the refractive index is a function of the angle of incidence, and therefore, the appropriate value for the average refractive index must be used in the foregoing formulations. However, for uniaxial crystals (such as lithium niobate), if the crystal is oriented in such a way that its optic axis is parallel to the x axis for the geometry used in this paper (Fig. 1), birefringence appears only in the case of E-mode polarization. In addition, since the amplitude of the spatial modulation of the refractive index would be 10^{-4} or smaller, the error in determining the grating profile is negligible due to the very small variations in the birefringence at different Bragg angles. For example, in the case of lithium niobate at $\lambda' = 514.5$ nm, changes in the amplitude of the fundamental grating do not exceed one tenth of one percent (using $n_0 = 2.337$ and $n_E = 2.243$, where n_0 and n_E are the principal indices of refraction for ordinary and extraordinary waves, respectively).

VII. Conclusions

A method for determining the refractive index profile, the effective

electric field, and the physical processes in optically-induced thick phase gratings in linear electro-optic crystals has been presented. This method utilizes a knowledge of the allowed family of grating profiles and a knowledge of the modulation ratio during hologram recording and the fundamental and the higher-order diffraction efficiencies of the grating. Thus, simple external measurements reveal the internal properties of the grating.

Acknowledgments

The authors would like to thank R. Magnusson for his help with the experimental measurements and L. Young for a prepublication copy of Ref. 2.

References

*Work supported by the National Science Foundation and by the National Aeronautics and Space Administration.

[1]J. J. Amodei, RCA Rev. 32, 185 (1971).

[2]W. D. Cornish, M. G. Moharam, and L. Young, J. Appl. Phys. 47, (1976) (in press).

[3]G. A. Alphonse, R. C. Alig, D. L. Staebler, and W. Phillips, RCA Rev. 36, 213 (1975).

[4]S. F. Su and T. K. Gaylord, J. Appl. Phys. 46, 5208 (1975).

[5]D. L. Staebler and J. J. Amodei, J. Appl. Phys. 43, 1042 (1972).

[6]A. M. Glass, D. von der Linde, and T. J. Negran, Appl. Phys. Lett. 25, 233 (1974).

[7]S. F. Su and T. K. Gaylord, J. Opt. Soc. Am. 65, 59 (1975).

[8]These, of course, depend on the physical propertities of the recording materials. For example, for lithium niobate, it can be shown[9] that negative signs must be chosen for both $n_{s1}(u_1)$ and $n_{c1}(u_1)$ when the +c axis of the crystal is directed in the +x reference direction, and that the positive sign for $n_{s1}(u_1)$ and negative sign for $n_{c1}(u_1)$ must be chosen when the +c axis is directed in the -x reference direction. No matter which direction (+x or -x) is chosen for the +c axis direction, the same refractive index profile in the lithium niobate crystal is obtained. This shows that there is no ambiguity in the solution.

[9]S. F. Su, Ph.D. thesis, Georgia Institute of Technology, 1976.

[10]H. Kogelnik, J. Opt. Soc. Am. 57, 431 (1967).

FIGURE CAPTIONS

Fig. 1 Geometry of thick grating showing recording beams. The spatial modulation of the refractive index is indicated by the line pattern.

Fig. 2 One grating period of the refractive index profile determined from diffraction efficiencies that are a) 5.0% too large and b) 5.0% too small compared to the actual profile.

Fig. 3 One grating period of the refractive index profile of a holographic grating recorded in a 2.12-mm-thick iron-doped lithium niobate crystal.

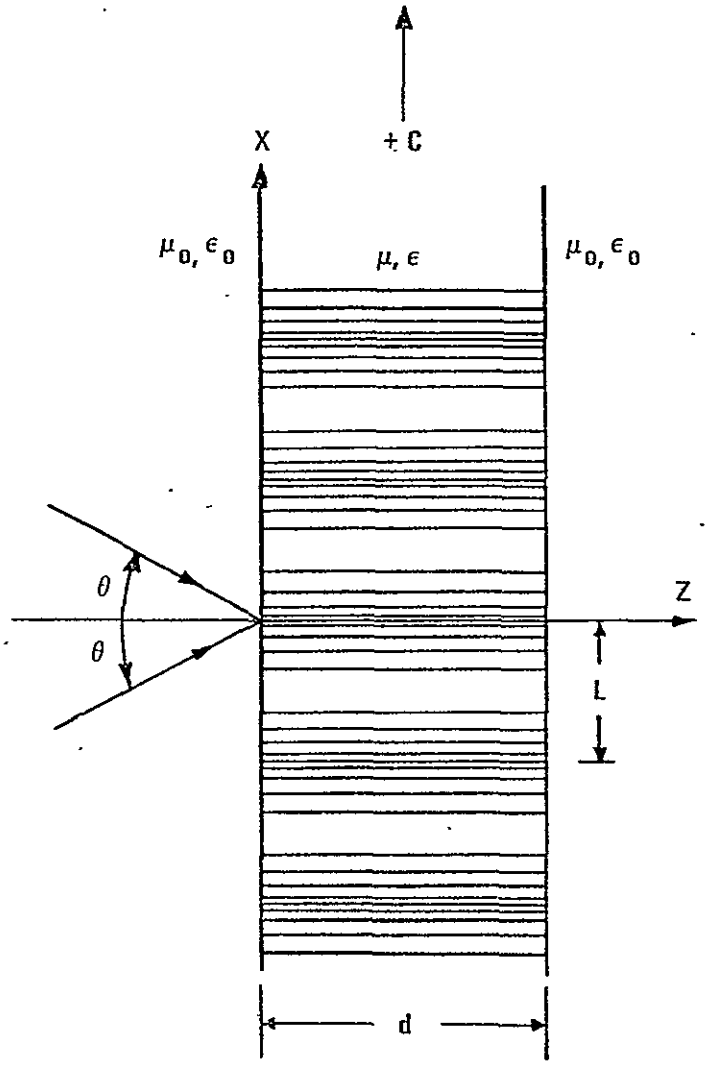

Fig. 1 Geometry of thick grating showing recording beams. The spatial modulation of the refractive index is indicated by the line pattern.

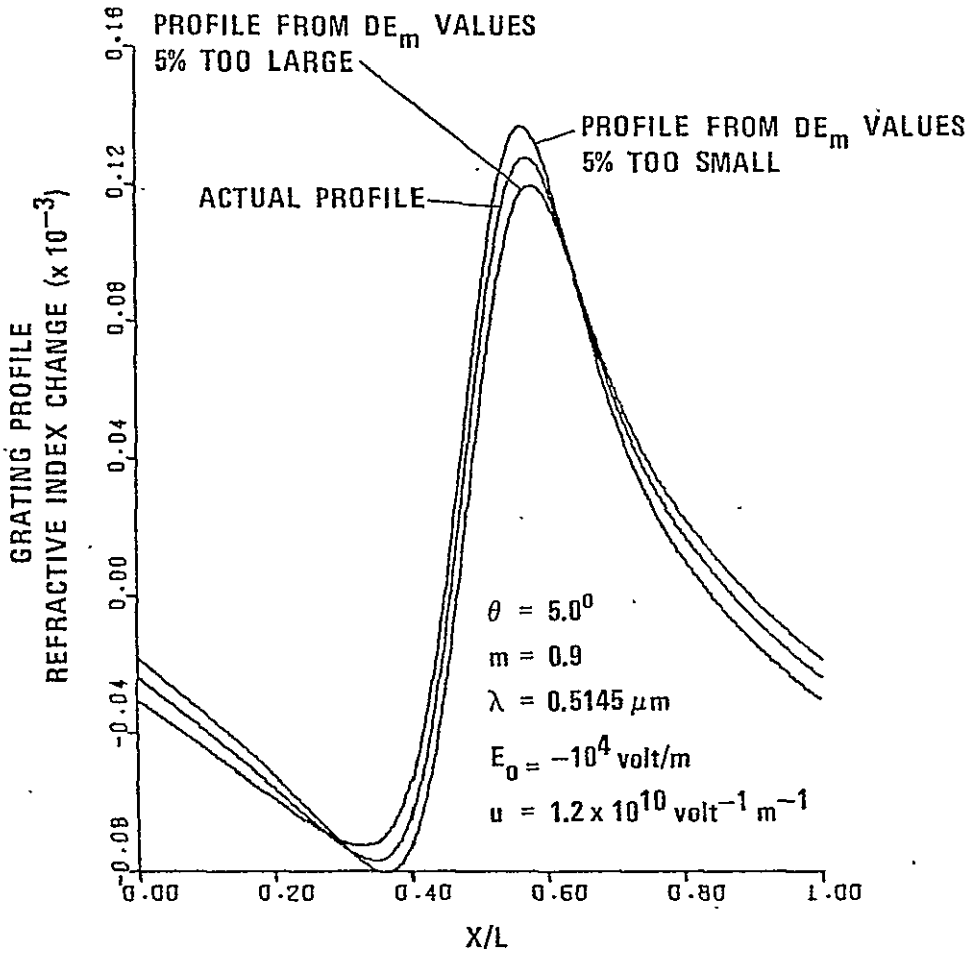

Fig. 2 One grating period of the refractive index profile determined from diffraction efficiencies that are a) 5.0% too large and b) 5.0% too small compared to the actual profile.

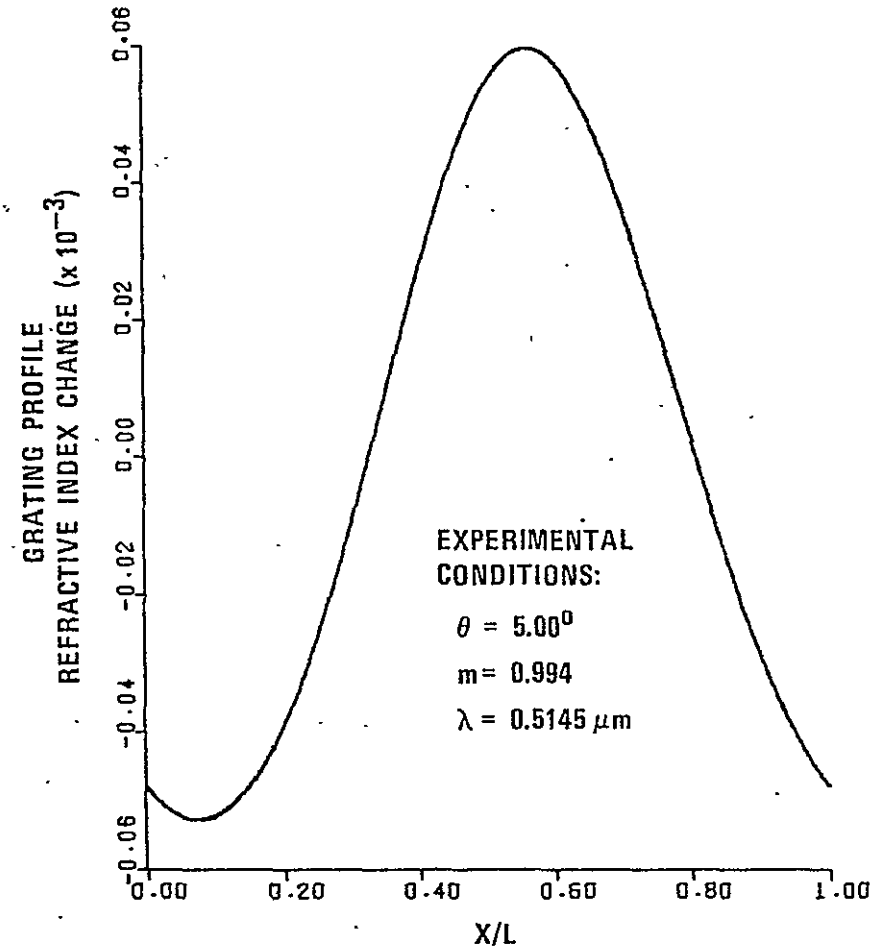

Fig. 3 One grating period of the refractive index profile of a holographic grating recorded in a 2.12-mm-thick iron-doped lithium niobate crystal.

TABLE I. Comparison of the original Fourier components and the calculated Fourier components of the gratings generated through diffusion of electrons, drift of electrons, and a combination of the two. The grating parameters are $n_o = 2.243$ and $L = 3.6303$ μm.

Physical mechanism		Refractive Index Fourier Component (x 10^{-5})									
		n_{c1}	n_{s1}	n_{c2}	n_{s2}	n_{c3}	n_{s3}	n_{c4}	n_{s4}	n_{c5}	n_{s5}
Diffusion	Original	0.000	-6.842	0.000	4.216	0.000	-2.566	0.000	1.536	0.000	-0.900
	Calculated	0.000	-6.842	0.000	4.216	0.000	-2.566	0.000	1.536	0.000	-0.899
Drift	Original	-4.997	0.000	2.988	0.000	-1.755	0.000	1.009	0.000	-0.566	0.000
	Calculated	-4.997	0.000	2.988	0.000	-1.755	0.000	1.009	0.000	-0.566	0.000
Diffusion & Drift	Original	-4.997	-6.842	2.988	4.216	-1.755	-2.566	1.009	1.536	-0.566	-0.900
	Calculated	-4.997	-6.842	2.988	4.216	-1.755	-2.566	1.009	1.536	-0.566	-0.899

III. DYNAMIC ANALYSIS OF THE RECORDING AND READING OF VOLUME HOLOGRAMS

Static diffraction characteristics of thick gratings have been analyzed by Burckhardt [5] by solving the exact electromagnetic boundary-value problem and by Kogelnik [6] by employing a coupled-wave theory. In these theories, the thick grating is assumed to exist already and is not affected by the reconstruction process. The grating is assumed to be uniform through the thickness of the material. Much experimentally observed behavior only can be explained by a dynamical theory that allows the interference of an incident light beam with its own diffracted beam inside the material. The results of the dynamical theory developed by Magnusson and Gaylord are included in Reference [7], which is reproduced on the following pages of this report.

Use of dynamic theory to describe experimental results from volume holography*

R. Magnusson and T. K. Gaylord

School of Electrical Engineering, Georgia Institute of Technology, Atlanta, Georgia 30332
(Received 1 July 1975)

The general applicability of dynamic theory to the description of the recording and readout characteristics of volume (thick) hologram gratings is indicated. In dynamic theory (as opposed to static theory), the volume nature of the thick holographic grating allows the interference of an incident light beam with its own diffracted beam inside the recording medium. This effect causes the continuous recording of another grating that alters the initial one, producing a resultant grating that is not uniform through the thickness of the recording material and a grating whose writing and reading characteristics may vary dramatically depending on the recording material and the experimental conditions. A large number of diverse types of writing, reading, and angular selectivity behavior have been reported in the published literature The dynamic theory of thick hologram writing and reading is shown to predict qualitatively all of these various types of experimental behavior.

PACS numbers: 42.40 D, 42.30.N

I. INTRODUCTION

Thick gratings and thick holograms have numerous applications based on their properties of high diffraction efficiency,[1] wavelength selectivity,[1] angular selectivity,[1] and reduced noise.[2] Thick gratings may be used as highly efficient diffraction gratings, narrow-band spectral filters,[3] thick grating lenses,[4] imaging systems capable of spectral resolution of extended objects,[2] wave guides for surface waves,[5] frequency-selective grating reflectors for thin-film distributed feedback lasers,[6] thin-film waveguide couplers,[7,8] and as deflectors and modulators.[9] Thick (volume) holograms are of interest due to their use in high-capacity information storage,[10] color holography,[11] and in white light reconstruction of holograms.[12]

The static diffraction characteristics of a thick grating have been analyzed by Burckhardt[13] by solving the exact electromagnetic boundary-value problem and by Kogelnik[1] by employing a coupled-wave theory. In these theories, the thick grating is assumed to exist already (as opposed to analyzing the recording process); it is assumed to be uniform through the thickness of the material; and it is assumed to be unaffected by the reconstruction process. These theories have been applied successfully to a large number of experimental situations. There remain, however, numerous types of experimentally observed behavior that are not predicted with these static theories. These include certain writing effects, reading effects, and angular selectivity effects (to be discussed in this paper).

It has been recognized[14] that the volume nature of thick holograms permits the interference of an incident light beam with its own diffracted beam inside the recording medium. This effect causes the continuous recording of a new grating that may add to or subtract from the initial grating producing a resultant grating that is not uniform through the thickness of the material. As is shown in this paper, the explanation of the resulting characteristics, in general, requires a dynamical theory such as that developed by Ninomiya.[15]

Among the materials used for recording volume holograms are those that exhibit light-induced refractive-index changes (photorefractive materials), those that exhibit light-induced changes in optical absorption (photochromic materials), and those that exhibit both of these effects. Numerous recording materials exist in each of these categories.[16]

II. ANALYTICAL TECHNIQUES

The coupled-wave theory used here originated in acoustics.[17] This method has since been adapted to the analysis of volume holograms. Kogelnik[1] analyzed diffraction from sinusoidal hologram gratings and Su and Gaylord[18] analyzed nonsinusoidal gratings. These authors assumed the existence of a uniform grating through the thickness of the medium. Further, they assumed that the hologram grating can be addressed with a light beam without affecting the grating. Thus, these approaches are essentially static.

A more general approach, combining and extending the initial efforts of Kogelnik[1] and Kermisch,[19] has been presented by Ninomiya.[15] He included in the basic coupled-wave formalism, the dynamic behavior of holograms during recording and reading. That is, during recording, the development of the hologram continuously affects the diffraction process (feedback). Similarly, during reading, the incident beam is diffracted inside the medium and the resultant two beams interfere with each other producing changes which may either add to or subtract from the existing holographic grating.

There has been little study of the characteristics of hologram gratings that are not uniform in the direction perpendicular to the hologram surface. Kermisch[20] and Uchida[21] have theoretically analyzed the case of an exponentially attenuated grating, the latter using the coupled-wave approach. In the present work, nonuniformity is shown to occur for photorefractive materials as a result of the spatial phase difference (represented by ϕ_n) between the hologram-forming light interference pattern and the resulting index-of-refraction grating. Also, of course, an attenuated profile is produced if α_0, the average absorption coefficient of the material, is nonzero. It is found that the index profiles can have

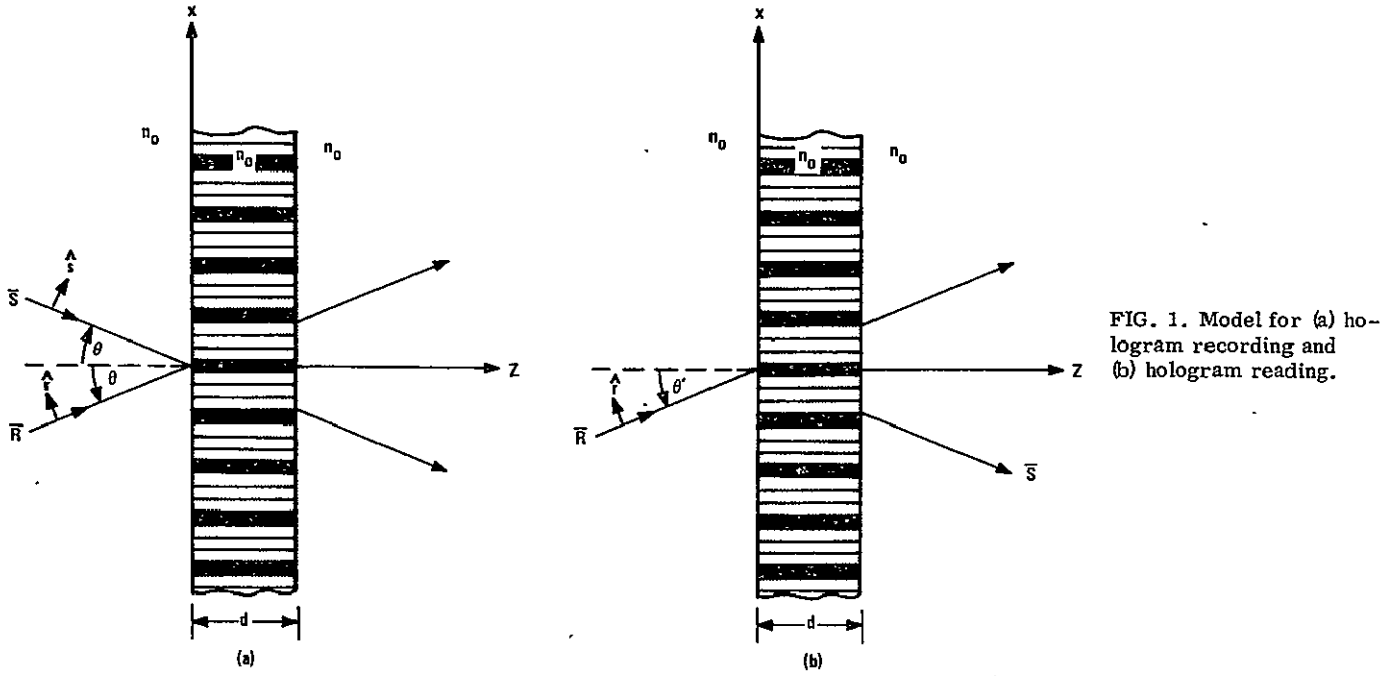

FIG. 1. Model for (a) hologram recording and (b) hologram reading.

many forms in addition to exponential. The above theories[1,15,18–21] have been presented without experimental results.

In this paper, the dynamical coupled-wave equations have been generalized to allow deviations in the angle of incidence and the wavelength, and are given for the E-mode polarization. These are then used to calculate the grating profiles and the writing, reading, and angular selectivity characteristics of unslanted phase volume holograms. Numerous types of experimental behavior cited in the literature as well as new experimental results presented here are shown to be predicted by the dynamical theory.

III. MODEL AND DYNAMIC THEORY

A. Model

The thick hologram gratings treated here are assumed to be recorded by the intersection of two coherent light waves in a thick photosensitive medium. They are read by a single wave incident upon the hologram. The recording and reading configurations are shown in Fig. 1. The signal and reference beams represented by the vectors $\mathbf{S}$ and $\mathbf{R}$, respectively, are taken to be infinite plane waves. They are polarized in the plane of incidence of the grating (E mode) with polarization vectors $\hat{\mathbf{s}}$ and $\hat{\mathbf{r}}$. The medium is unbounded in the x and y directions. It is to be noted that, during recording, the waves are symmetric in their angle of incidence and, therefore, the grating fringes are normal to the material surface (unslanted). The extension to slanted gratings is straightforward but little additional insight is gained. For convenience, it is assumed that the same average refractive index exists inside and outside the grating (this is a common simplification; see, e.g., Ref. 1) and thus no reflections or deviations occur.

B. Equations

Ninomiya[15] developed the dynamic coupled-wave equations that describe the writing, reading, and erasure of thick holograms for exact Bragg conditons and H-mode polarization ($\hat{\mathbf{s}} \| \hat{\mathbf{r}}$). Here the dynamical equations for E-mode polarization (electric field in the plane of incidence) are used because the available experimental data are primarily for the E-mode configuration. In addition, the equations have been generalized to permit deviations in the incident angle from the writing angle and deviations in the wavelength from the writing wavelength. The notation used here is that of Ninomiya.[15]

Following Ninomiya's development, the wave equation for the total electric field,

$$\nabla^2\mathbf{E} - \nabla(\nabla \cdot \mathbf{E}) + K^2\mathbf{E} = 0, \tag{1}$$

where K is the propagation constant, is used as a starting point. The total electric field in the grating may now be expressed by the vector

$$\mathbf{E}(\mathbf{r},t) = \mathbf{R}(\mathbf{r},t)\exp(-j\rho \cdot \mathbf{r}) + \mathbf{S}(\mathbf{r},t)\exp(-j\sigma \cdot \mathbf{r}), \tag{2}$$

where ρ and σ are the wave vectors of the reference and signal beams, respectively, and $\mathbf{r} = (x,y,z)$. The exposure is thus $\int_0^T \mathbf{E} \cdot \mathbf{E}^* dt$, where t is time and T is exposure time. From Eqs. (1) and (2), the following coupled equations are obtained for the wave amplitudes R and S (functions of z and t):

$$\cos\theta \frac{\partial R}{\partial z} + \gamma R = -j\Gamma_1 S(\hat{\mathbf{r}} \cdot \hat{\mathbf{s}})^2, \tag{3}$$

$$\cos\theta \frac{\partial S}{\partial z} + (\gamma + j\vartheta)S = -j\Gamma_2 R(\hat{\mathbf{r}} \cdot \hat{\mathbf{s}})^2, \tag{4}$$

where

$$\gamma = (j2\pi a/\lambda + b)\int_0^T (RR^* + SS^*)\,dt + \alpha_0, \tag{5}$$

$$\Gamma_1 = [(2\pi a/\lambda)\exp(j\phi_n) - jb\exp(j\phi_\alpha)]\int_0^T RS^*\,dt, \tag{6}$$

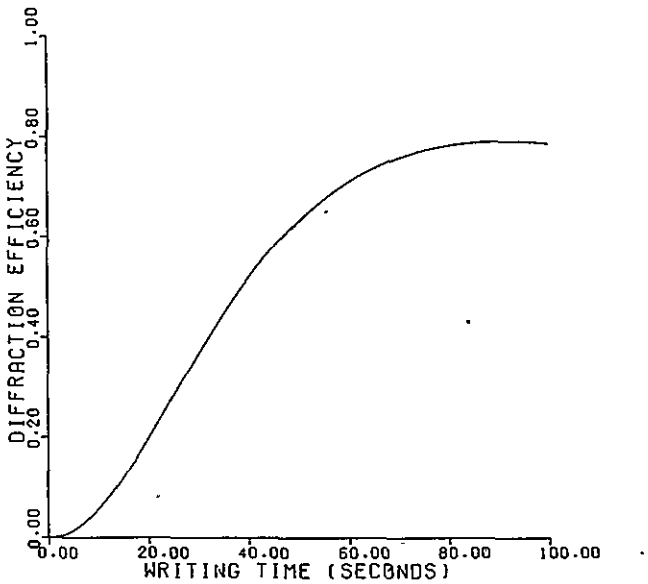

FIG. 2. Calculated hologram writing characteristic exhibiting a saturationlike appearance. Hologram thickness is 2.00 mm, $a=10^{-12}$ $(V/m)^{-2}$ sec^{-1}, $\phi_n=90°$, $\alpha_0=0$, and other parameters as given in Sec. IV.

$$\Gamma_2=[(2\pi a/\lambda)\exp(-j\phi_n)-jb\exp(-j\phi_\alpha)]\int_0^T SR^*\,dt, \quad (7)$$

$$\vartheta=(\beta_0^2-\sigma'^2)/2\beta_0, \quad (8)$$

$$\beta_0=2\pi n_0/\lambda, \quad (9)$$

$$\hat{r}\cdot\hat{s}=\cos 2\theta, \quad (10)$$

and λ is the free-space wavelength, n_0 is the average index of refraction, α_0 is the average absorption constant, ϕ_n and ϕ_α are the phase differences between the hologram-forming light interference pattern and the resulting refractive-index and absorption gratings, respectively, and a and b are the exposure sensitivities of the refractive-index changes and absorption changes, respectively. The quantity ϑ is the dephasing factor introduced by Kogelnik.[1] The magnitude of the propagation vector of the diffracted wave upon reading is

$$\sigma'=(\beta_\delta^2-4\beta_0\beta_\delta\sin\theta\sin\theta'+4\beta_0^2\sin^2\theta)^{1/2}, \quad (11)$$

where $\beta_\delta=2\pi n_\delta/\lambda'$. The primed quantities represent the values associated with the reading process.

Equations (3) and (4) can be solved numerically on a digital computer. It is shown that the solutions thus obtained qualitatively describe the various types of externally measurable diffraction behavior of volume holograms that have been experimentally measured and reported in the literature (sometimes with very little explanation).

IV. CALCULATED RESULTS AND EXPERIMENTAL BEHAVIOR

A. Calculational procedure

In this section, numerical results obtained by solving Eqs. (3) and (4) are presented for selected sets of hologram parameters. The solutions are seen to compare favorably with published experimental results. For writing, the equations are solved with $\vartheta=0$ (no dephasing) and the boundary conditions $R(0,t)=R_0$ and $S(0,t)=S_0$. For reading, ϑ can be nonzero. Deviations in wavelength and/or incident angle from the corresponding writing quantities result in $\vartheta\neq 0$. The boundary conditions $R(0,t)=R_\delta$ and $S(0,t)=0$ are used for the case of readout with the R beam and $R(0,t)=0$ and $S(0,t)=S_\delta$ are used for readout with the S beam. Diffraction efficiency is then defined as $\eta=S(1,T)S^*(1,T)/R_\delta^2$ for R-beam readout and $\eta=R(1,T)R^*(1,T)/S_0^2$ for S-beam readout.

The computer algorithm employs a fourth-order Runge-Kutta method to solve the equations with respect to the z variable. The integrations in t were performed by replacing the integrals by the corresponding sums and using increments, Δt, small enough for convergence. The actual incremental step sizes used were $\Delta z=0.01$ (the equations are normalized with respect to the thickness so that $0\leq z\leq 1$) and $\Delta t=0.5$ sec. The numerical accuracy was tested by decreasing the step sizes Δz and Δt until the improvements in convergence were insignificant.

The calculations presented are for a 1.66- and a 2.00-mm-thick crystal of $LiNbO_3$ with its optic axis (c axis) in the plane of incidence of the writing beams. The writing and reading waves are polarized in the plane of incidence and have a wavelength of $\lambda=0.5145$ μm. The angles of incidence for the writing beams are $\pm 2.23°$ (corresponding to external angles of incidence of $\pm 5.00°$ for the grating surrounded by a unity refractive-index medium). For this wavelength, polarization, angle of incidence, and orientation of the lithium niobate crystal, the index of refraction is $n_0=2.2426$. For writing $R_0=S_0=1000$ V/m. Reading is done with $R_\delta=1000$ V/m. Only transmission phase holograms are considered, that is, b is set equal to zero (no photochromic effect).

B. Writing

With a few exceptions, the experimental diffraction efficiency writing characteristics (η vs t) reported in the literature for volume holograms begin with zero initial slope and increase in a parabolic fashion. The magnitudes of the diffraction efficiencies reported, however, vary considerably. Several workers[22–25] report relatively low efficiencies (e.g., $<1\%$) exhibiting saturating behavior or a very small rate of increase. Others[26–31] have reported higher efficiencies, also showing saturation behavior. At times, instead of saturation, an oscillatory diffraction efficiency is observed.[2,27,28,30,31] It seems that experimental oscillatory writing characteristics are observed primarily for relatively high-efficiency holograms. In many papers,[2,14,24,27,32–38] the writing is terminated before the onset of oscillation or saturation.

The types of behavior indicated above can be straightforwardly predicted using the dynamic theory. The oscillatory behavior is seen to be inherent in the theory because of the assumption of constant refractive-index exposure sensitivity. The material is thus assumed to respond continuously to the interaction of the wave fields at all times. Physically, the quantity a may be time depen-

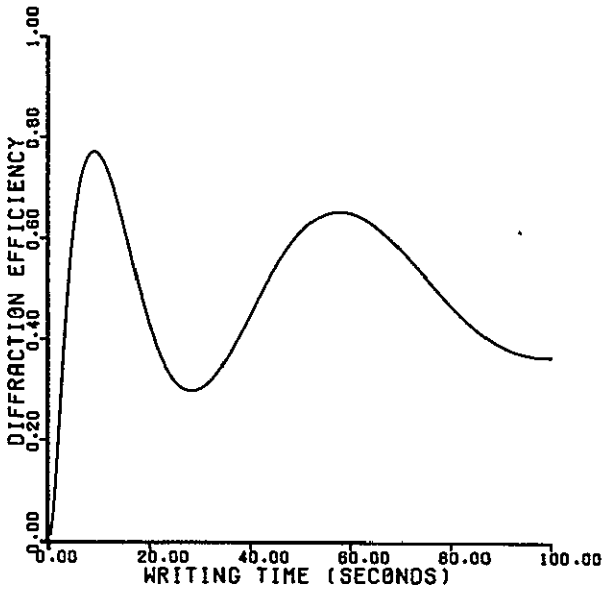

FIG. 3. Calculated oscillatory hologram writing characteristic with decreasing amplitude and increasing period of the diffraction efficiency oscillations. Hologram thickness is 2.00 mm, $\alpha = 10^{-11}$ $(V/m)^{-2}$ sec^{-1}, $\phi_n = 90°$, $\alpha_0 = 0$, and other parameters as given in Sec. IV.

dent since the physical mechanism(s) (such as photochemical effects, drift of charge carriers, diffusion of charge carriers, etc.) that produce the sensitivity may be self-limiting in some materials. Therefore, saturation at low or high efficiency may be brought about by a vanishing sensitivity. At the turning point toward saturation, $|d\eta/dt|$ is strongly affected by $|da/dt|$. Thus, depending on the material and the experimental situation, gradual[22,24–28,30,31] or abrupt[23,29] turning points are observed in $\eta(t)$. Figure 2 demonstrates that an approximately saturating behavior may be predicted by the dynamic equations even with a constant refractive-index exposure sensitivity (Fig. 2 is similar to Fig. 6 in Ref. 15). Calculated oscillatory behavior is shown in Fig. 3. Figure 3 exhibits behavior similar to that experimentally observed by the authors in lithium niobate and shown in Fig. 4. Note the decreasing amplitude and increasing period of the diffraction efficiency oscillations with exposure in both of these figures. Figure 3 also bears qualitative resemblance to Fig. 6 in Ref. 27 and to Fig. 2 in Ref. 28. Figure 5 illustrates large increasing diffraction efficiency oscillations with minima near 0%. This behavior is like that depicted in Fig. 5 of Ref. 2 for a 1.8-mm-thick photopolymer hologram grating.

The exceptional cases for which writing starts with an apparently linear $\eta(t)$ characteristic[23,25,28,39] (rather than parabolic) may possibly be reconciled by the fact that the zero-slope initial portion of the $\eta(t)$ is sometimes of very brief duration (see, for example, Fig. 4 of this paper, Fig. 2 in Ref. 22, Fig. 5 in Ref. 27, Fig. 1 in Ref. 35, etc.), and thus the curve appears to be approximately linear when in fact it may not be.

C. Reading

The application of a reading beam to a thick hologram may continually change its characteristics. Experimentally, the most commonly observed result seems to be exponentiallike decay of the diffraction efficiency.[14,22–24,27,28,30,32–34,36,37,40,41] Oscillatory diffraction efficiency readout behavior has also been reported. In rhodium-doped $LiNbO_3$, for example, vivid oscillations have been observed during readout.[28] An iron-doped sample of $LiNbO_3$ has shown an initial rise and a subsequent decay of diffraction efficiency upon readout.[33] Oscillatory behavior at low efficiency following an exponentiallike decay has also been noted.[33] Self-enhancement (an increase of diffraction efficiency upon reading) of Fe-doped $LiNbO_3$ holograms has been observed.[42] In this case, erasure and enhancement were produced depending on which of the original writing beams was used for readout. Behavior such as this has been theoretically predicted by Staebler and Amodei.[14] We present here further experimental results for volume holograms that show this type and other effects upon

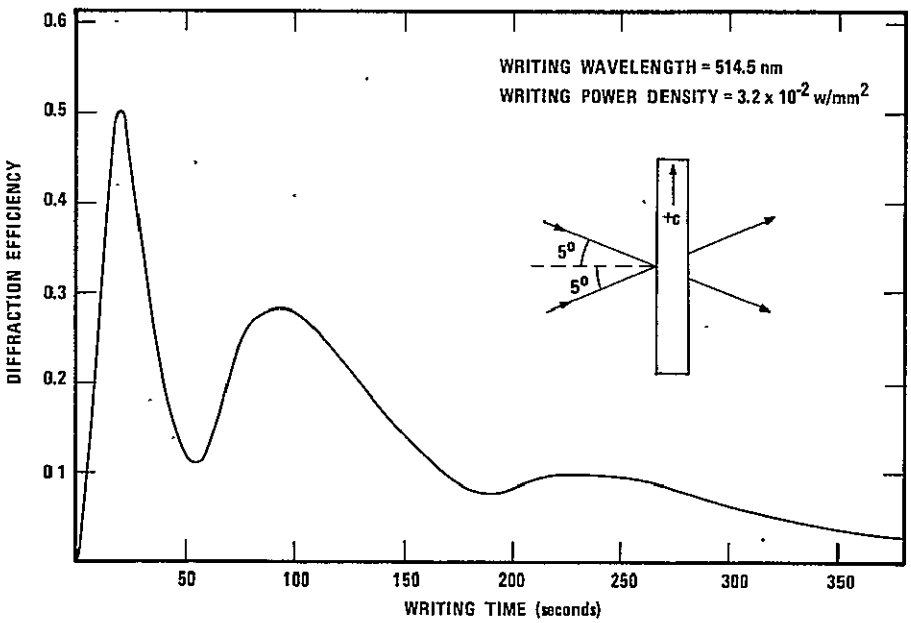

FIG. 4. Experimental oscillatory hologram writing characteristic for a 1.66-mm-thick iron-doped lithium niobate crystal. Writing beam polarizations are in the plane of incidence and the experimental configuration is as shown in the figure inset.

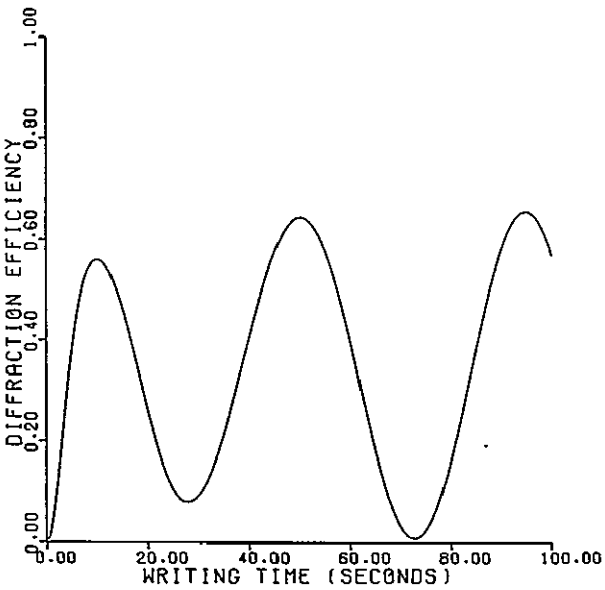

FIG. 5. Calculated oscillatory hologram writing characteristic with diffraction efficiency minima near 0%. Hologram thickness is 2.00 mm, $a=10^{-11}$ $(V/m)^{-2}$ sec^{-1}, $\phi_n=60°$, $\alpha_0=10^2$ m^{-1}, and other parameters as given in Sec. IV.

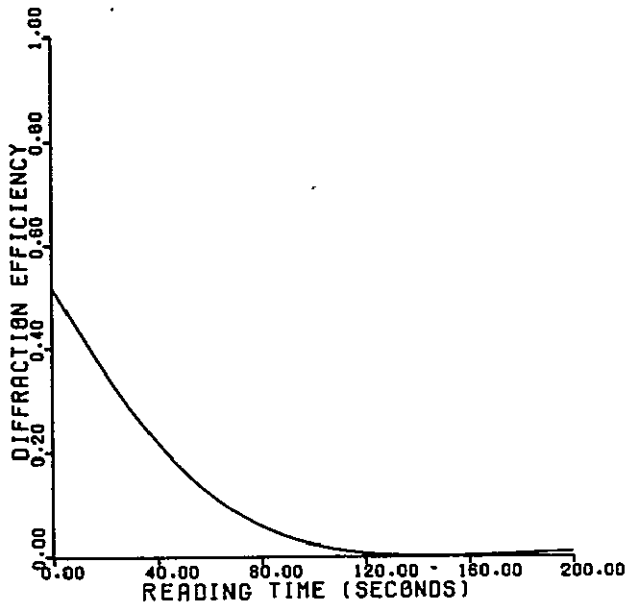

FIG. 6. Calculated exponentiallike reading characteristic. Note slight rise in efficiency at a reading time of 200 sec. Hologram thickness is 2.00 mm, $a=10^{-12}$ $(V/m)^{-2}$ sec^{-1}, $\phi_n=90°$, $\alpha_0=0$, readout with R beam, and other parameters as given in Sec. IV. The original hologram was recorded using these same parameters and an exposure time of 40 sec.

changing the reading beam from the R beam to the S beam (see Fig. 1).

The various types of behavior discussed above are all predicted by the dynamic theory. In Fig. 6, for example, a calculated exponentiallike decay of the hologram efficiency is shown. Note that, eventually, the efficiency rises again (as experimentally reported in Ref. 33 and in Fig. 4 of Ref. 41). Figure 7 depicts the experimentally recorded decay of the efficiency of a hologram written in a 1.66-mm-thick iron-doped crystal of $LiNbO_3$ for the beam configuration indicated in the inset of Fig. 7. Note the slight oscillations at low efficiency. Figures 8 and 9 illustrate the calculated effect of switching the reading beam to the symmetrical angular location. In Fig. 8, an initial decrease in diffraction efficiency is predicted, whereas in Fig. 9 an initial increase is predicted (like experimental data in Fig. 6 of Ref. 33, in Fig. 2 of Ref. 42, and in Fig. 12 of this paper). Figure 8 also clearly predicts oscillations at low efficiency such as have been experimentally observed. Figure 10 shows the behavior of efficiency oscillations followed by monotonic decay as calculated by the dynamic theory. This is qualitatively like the experimental readout behavior observed in rhodium-doped $LiNbO_3$ by Ishida *et al.*[28] Figure 11 illustrates calculated diffraction efficiency

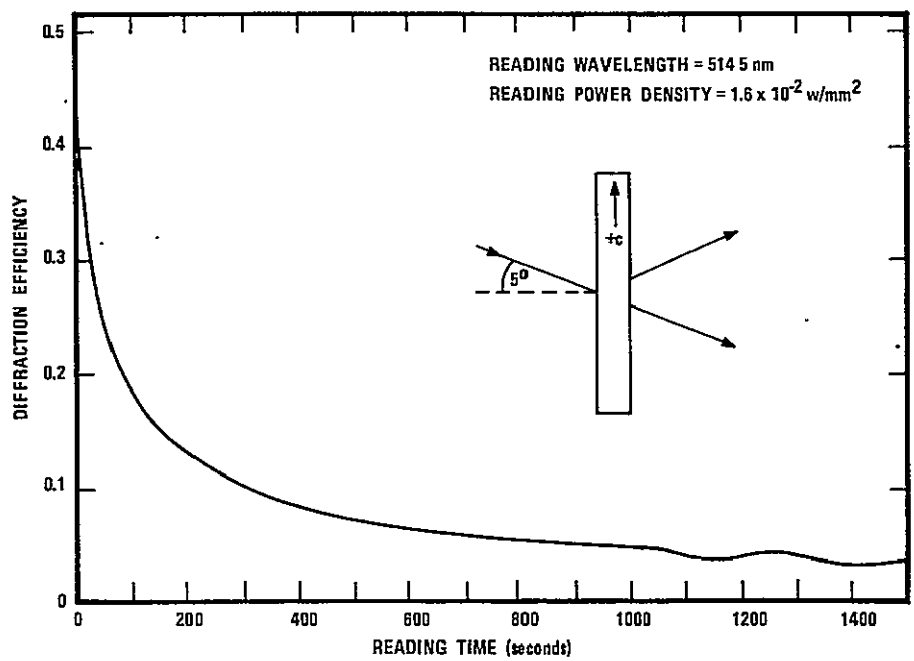

FIG. 7. Experimental exponentiallike reading characteristic for a 1.66-mm-thick iron-doped lithium niobate crystal. Small amplitude diffraction efficiency oscillations are present at low efficiencies. Reading beam polarization is in the plane of incidence and the experimental configuration is as shown in the figure inset.

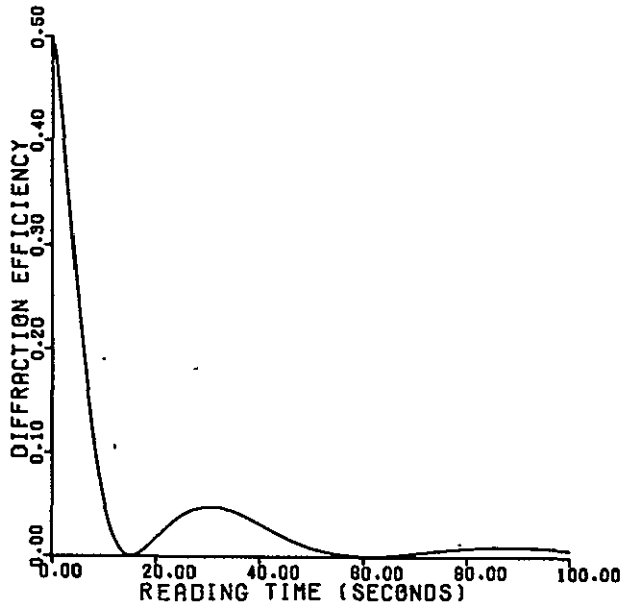

FIG. 8. Calculated reading characteristic showing diffraction efficiency oscillations at low efficiencies. Hologram thickness is 2.00 mm, $a=10^{-11}$ $(V/m)^{-2}$ sec^{-1}, $\phi_n=90°$, $\alpha_0=10^2$ m^{-1}, readout with R beam, and other parameters as given in Sec. IV. The original hologram was recorded using these same parameters and an exposure time of 10 sec.

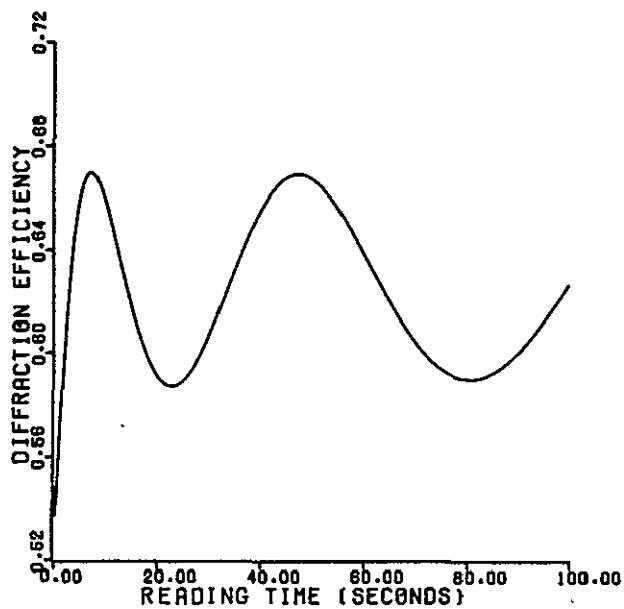

FIG. 9. Calculated enhancement and oscillatory reading characteristic resulting from S-beam readout as opposed to normal R-beam readout. All other conditions and parameters are identical to those of Fig. 8.

oscillations that both decrease and increase as a function of readout exposure. In Fig. 12, we show experimentally measured oscillatory reading behavior for the same hologram grating used in Fig. 7 except that reading is done with the beam at the symmetric recording angle (reading with the S beam instead of the R beam in the notation of Fig. 1). Large variations in both the amplitude and the period of the efficiency oscillations are observed. This behavior is qualitatively similar to the predicted readout diffraction efficiency of Fig. 11.

D. Angular selectivity

Angular selectivity refers to the variation of diffraction efficiency as a function of angle of incidence of the reading wave. In experiments measuring this property of thick hologram gratings, a low power reading beam or a reading beam of a wavelength at which the material is insensitive is generally used so as not to affect the hologram by the process of measurement.

Experimental angular selectivity results are somewhat less plentiful than the other terminally measured

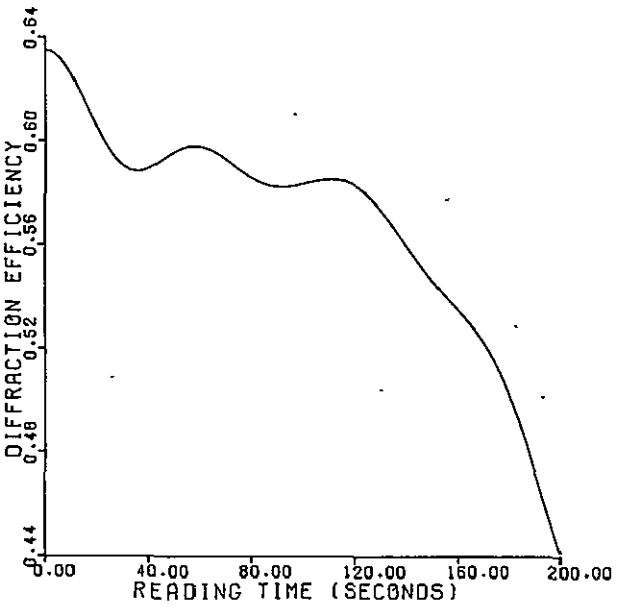

FIG. 10. Calculated reading characteristic showing diffraction efficiency oscillations followed by rapid decay. Hologram thickness is 2.00 mm, $a=10^{-11}$ $(V/m)^{-2}$ sec^{-1}, $\phi_n=0°$, $\alpha_0=0$, readout with R beam, and other parameters as given in Sec. IV. The original hologram was recorded using these same parameters and an exposure time of 35 sec.

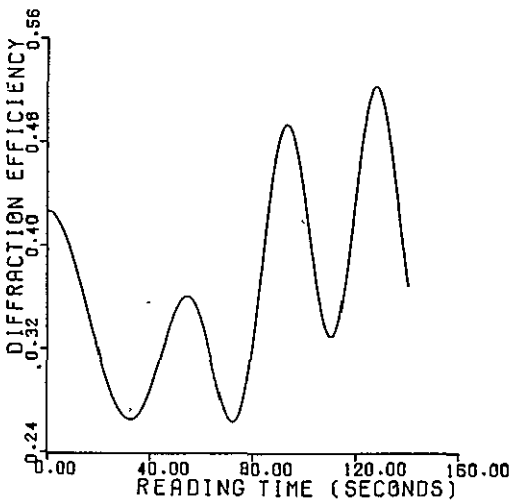

FIG. 11. Calculated oscillatory reading characteristic showing large variations in the amplitude and period of the diffraction efficiency oscillations. Hologram thickness is 2.00 mm, $a=10^{-11}$ $(V/m)^{-2}$ sec^{-1}, $\phi_n=0°$, $\alpha_0=0$, readout with R beam, and other parameters as given in Sec. IV. The original hologram was recorded using these same parameters and an exposure time of 10 sec.

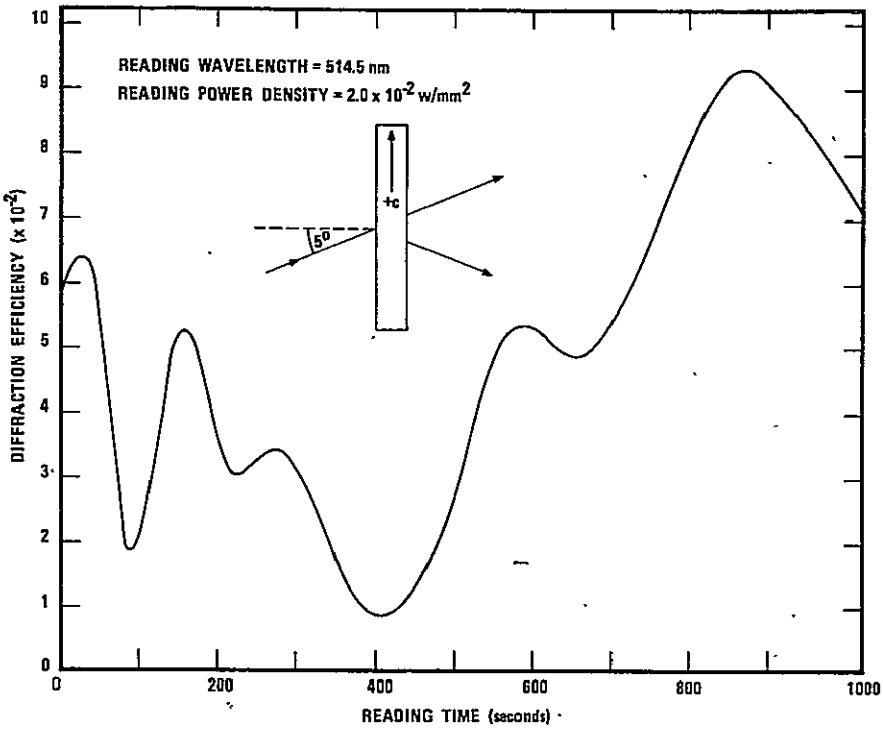

FIG. 12. Experimental oscillatory reading characteristic for a 1.66-mm-thick iron-doped lithium niobate crystal. A wide variation in the amplitude and period of the diffraction efficiency oscillations is apparent. Reading beam polarization is in the plane of incidence and the experimental configuration is as shown in the figure inset.

characteristics of thick holograms. Some of the existing experimental results exhibit a series of nonzero minima in place of the nulls [43–47] predicted by static hologram theories. Some experimental data show no minima in the angular selectivity. [43,48] It is now well established [20,21,43] that nonuniformity of the grating with material thickness produces nonzero diffraction minima or the complete disappearance of the minima in the angular selectivity.

The dynamic theory straightforwardly predicts the various types of angular selectivity behavior of volume holograms. Here, grating nonuniformity arises if $\phi_n \neq 0$, or $\alpha_0 \neq 0$, or if both ϕ_n and α_0 are nonzero. Nonuniformity, and the corresponding disappearance of angular selectivity minima for low-loss materials ($\alpha_0 \cong 0$), is explained here by the dynamic theory but cannot be explained by the static theories. In Fig. 13, a logarithmic plot of experimental data is presented for a hologram written in a 1.66-mm-thick 0.05-mole% Fe-doped crystal of $LiNbO_3$ and compared to the solution of Eqs. (3) and (4) for the same conditions. Due to the short writing time and the low efficiency ($\cong 1\%$), the grating is still quite uniform through the thickness of the material (z direction) and thus the grating exhibits well-defined nulls in the diffraction efficiency for a series of reading angles. Theory and experiment both show these nulls. Figure 14 indicates the vanishing of the angular selectivity nulls as the grating develops and begins to show nonuniformity in the amplitude of the refractive index modulation with z (see inset in Fig. 14). Figure 15 shows the angular selectivity and the index profile for the hologram grating after further exposure. Note that $\alpha_0 = 0$. Figure 15 illustrates that the absolute maximum diffraction intensity peak now occurs off the Bragg angle. The pattern is symmetric with respect to the Bragg angle and thus a second peak occurs for an angle of incidence on the other side of the Bragg angle.

V. DISCUSSION

The prediction of a very wide variety of results in volume holography is possible with the dynamic theory. Writing and reading characteristic curves (usually presented as η vs t) may have an infinitude of possible magnitudes and shapes. The calculated curves presented in this paper are typical results taken from a much larger number of cases that have been analyzed by the authors. Many rapidly varying experimental writing and reading results (such as the data shown in Fig. 12) have previously informally been attributed to "experimental problems". It is now apparent that these types of oscillatory results are "normal" and are to be expected.

The dynamic theory is an important aid in identifying the "significant" parameters in volume holographic recording and readout. Relatively few parameters are needed in the dynamic theory. The role of each of these parameters can be determined in a given situation. This indicates the possibility of using the dynamic theory (1) as an aid in synthesis and (2) as a diagnostic tool.

As an aid in synthesis, the dynamic theory serves as an indicator of the parameter values that are needed to produce a particular desired situation (e.g., uniformity of induced change through the thickness of a hologram, a certain type of angular selectivity, an enhancing readout, a rapidly erasing readout, etc.). The dynamic theory parameters in some materials, indeed, may be controlled in a fairly direct manner. For example, in iron-doped lithium niobate, α_0 and a may be dramatically changed by heat treating the material in various environments. [32,33] Microscopically, this has been shown to control the relative Fe^{2+} and Fe^{3+} concentrations in iron-doped lithium niobate. [32,33] In addition, the phase difference between the light and the refractive-index

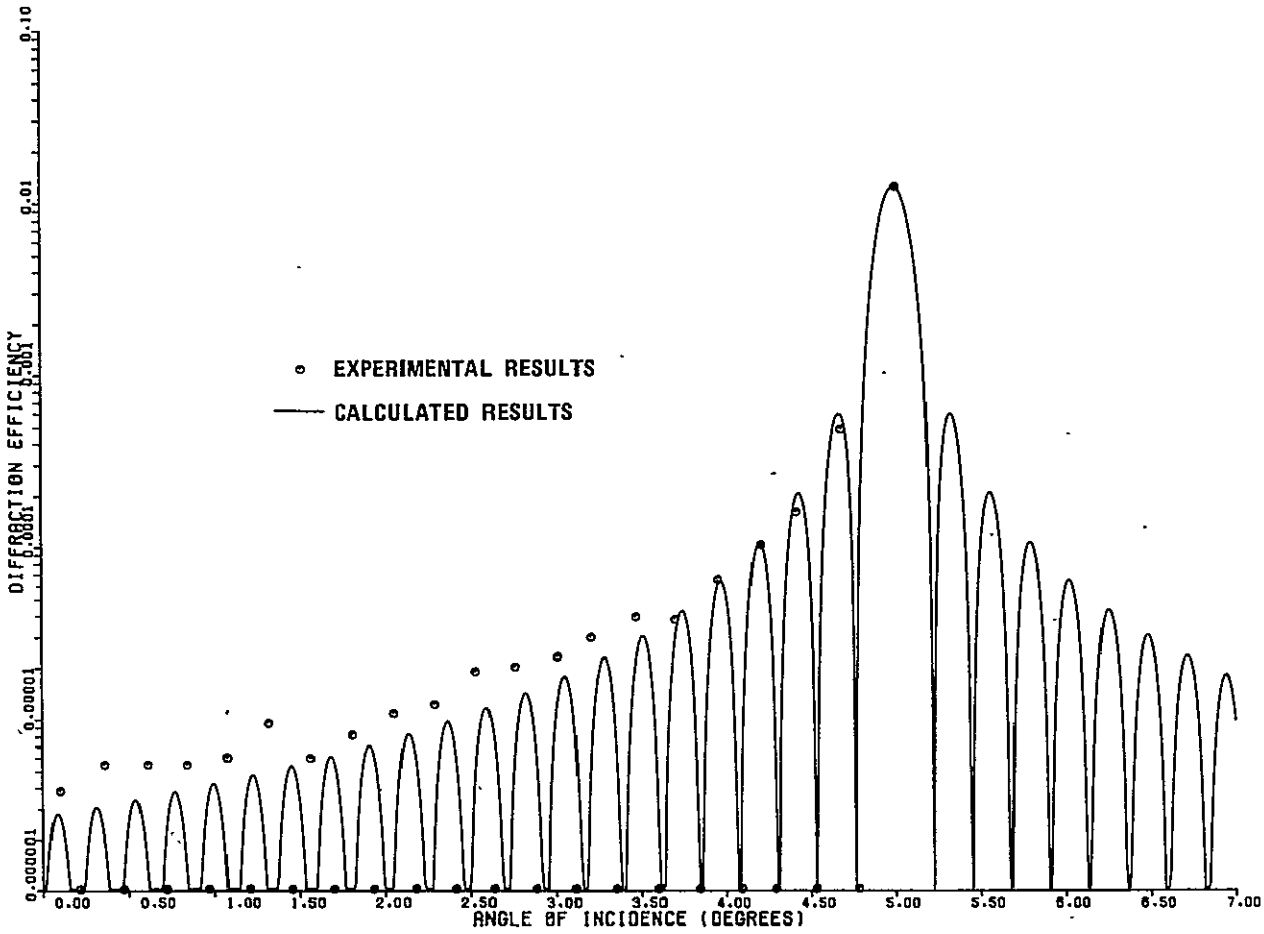

FIG. 13. Experimental and calculated angular selectivity exhibiting zero diffraction efficiency at minima. The hologram is a 1.66-mm-thick iron-doped lithium niobate crystal. Experimentally, hologram was written with a wavelength of 514.5 nm, a total power density of 3.5 mw/mm^2, external angles of incidence of $\pm$ 5.00°, a writing time of 5 sec, polarization in the plane of incidence, and the configuration shown in the inset of Fig. 4. Experimentally, the angular selectivity was measured with a low power beam of the same wavelength. The calculated curve is for a hologram of thickness of 1.66 mm, written with $R_0 = 571$ V/m, $S_0 = 518$ V/m, for 5 sec with $a = 3.8 \times 10^{-12}$ (V/m)$^{-2}$ sec^{-1}, $\phi_n = 0°$, and $\alpha_0 = 0$, these parameters being estimated from the experimental conditions.

grating, ϕ_n, approaches 0° when drift of the photoexcited electrons dominates[14] (which may be induced by externally applying an electric field). The phase difference approaches 90° when diffusion of the electrons dominates[14] (which may be induced by using a small fundamental grating spacing).

As a diagnostic tool, the dynamic theory, when coupled with experiment, is capable of determining certain material and hologram characteristics. By experimentally holding constant some of the dynamic theory parameters, other parameters and properties may be found. For example, the variations with grating thickness of the refractive index may be determined knowing the conditions of recording. This would allow the direct determination of the index profile (in the z direction) as opposed to assuming a uniform grating or an exponential variation with thickness (both of which may be totally incorrect). As another example, the variation with exposure of the refractive-index exposure sensitivity, a, may be measured. By holding the other dynamic theory parameters constant and measuring the hologram writing characteristic, the time dependence of the index exposure sensitivity may be determined. Chronologically, in the literature, the earlier thick recording materials tended to show a saturating-type writing characteristic indicating a rapidly decreasing value of a. More recently, higher-sensitivity materials have tended to show an oscillatory writing characteristic indicating a larger dynamic range for these materials (and thus the dynamic theory is valid in these cases with essentially a constant value of a).

VI. CONCLUSION

A large number of different types of recording and reading behaviors have been reported for thick (volume) holograms in a wide variety of recording materials. Writing, reading, and angular selectivity experimental data from approximately 25 published articles are cited in this paper as being representative of the known types of behavior. The dynamic theory of thick hologram recording and reading qualitatively predicts all of these various types of experimental behavior. Thus, the dynamic theory is potentially very powerful (1) in determining the material and recording parameters needed to produce a certain desired hologram characteristic

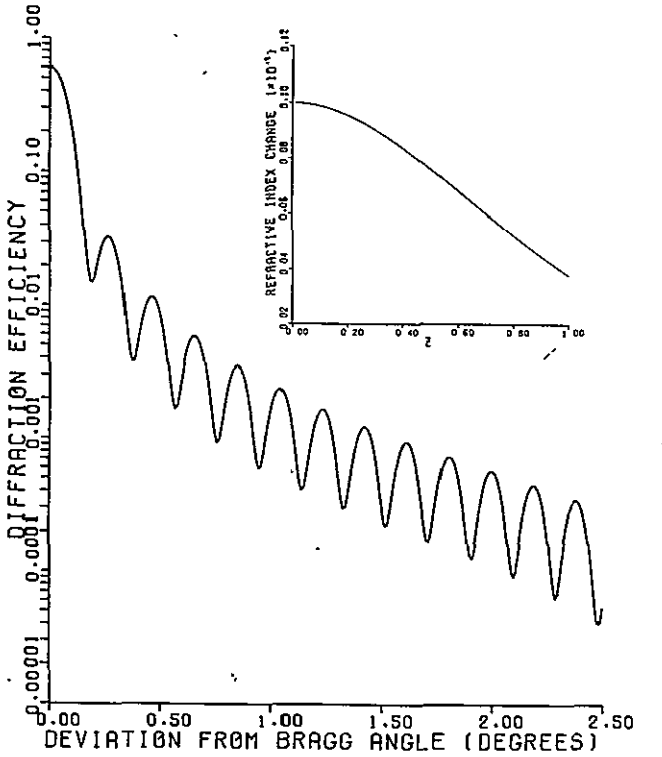

FIG. 14. Calculated angular selectivity exhibiting nonzero diffraction efficiency at minima. Nonzero minima are characteristic of phase holographic gratings having a variation in index of refraction through the thickness of the material. The refractive-index profile is shown in the inset. Hologram thickness is 2.00 mm, $\alpha = 10^{-11}$ $(V/m)^{-2}$ sec^{-1}, $\phi_n = 90°$, $\alpha_0 = 0$, and writing time is 5 sec.

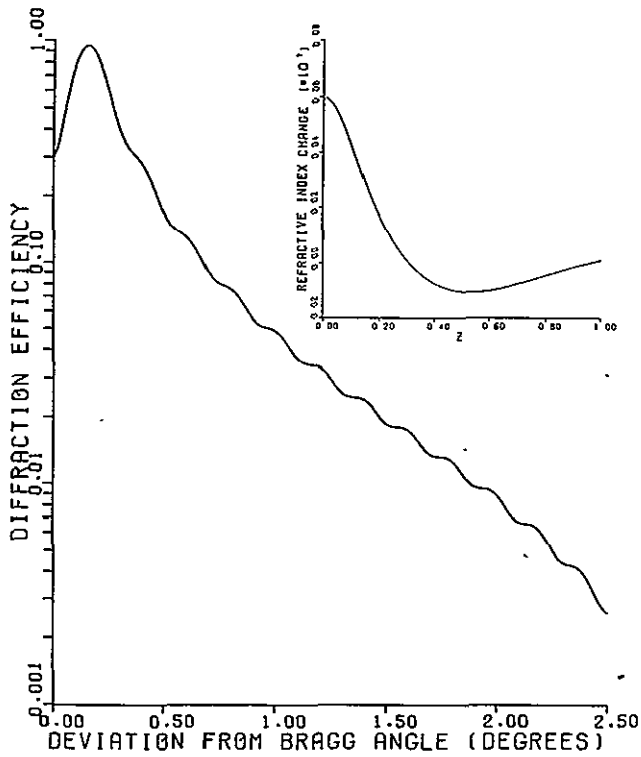

FIG. 15. Calculated angular selectivity showing the disappearance of diffraction efficiency minima. The same conditions as Fig. 14 prevail but with a longer writing time of 30 sec. The increased nonuniformity of the grating profile is shown in the inset.

and (2) as a diagnostic tool to analyze the parameters of thick photosensitive recording materials.

Note added in proof. An oscillatory diffraction efficiency upon readout has also been shown theoretically and experimentally to be possible due to changes in the multiple internal reflections as a result of crystal thermal expansion caused by the absorption of laser light. These results are reported in the work by W.D. Cornish and L. Young, J. Appl. Phys. 46, 1252 (1975). In our experimental case (Figs. 4, 7, 12, and 13), we have found by the reflectance test given in the above reference that our crystals do not satisfy the flatness-and-parallelism requirements necessary for such effects to occur. Laser-induced thermal expansion, therefore, does not significantly affect our experimental results.

ACKNOWLEDGMENTS

The authors would like to thank S. F. Su for his help with the numerical analysis in this paper and W. R. Callen for his help with the experimental measurements.

*Work supported by the National Science Foundation and by the National Aeronautics and Space Administration.

[1]H. Kogelnik, Bell Syst. Tech. J. 48, 2909 (1969).
[2]M.R.B. Forshaw, Opt. Laser Technol. 6, 28 (1974).
[3]B. H. Crawford, J. Sci. Instrum. 31, 333 (1954).
[4]J. N. Latta and R. C. Fairchild, J. Opt. Soc. Am. 63, 487 (1973).
[5]R. Shubert and J. H. Harris, J. Opt. Soc. Am. 61, 154 (1971).
[6]H. Kogelnik and C. V. Shank, Appl. Phys. Lett. 18, 152 (1971).
[7]H. Kogelnik and T. P. Sosnowski, Bell Syst. Tech. J. 49, 1602 (1970).
[8]M. L. Dakss, L. Kuhn, P. F. Heidrich, and B. A. Scott, Appl. Phys. Lett. 16, 523 (1970).
[9]J. M. Hammer, Appl. Phys. Lett. 18, 147 (1971).
[10]P. J. Van Heerden, Appl. Opt. 2, 393 (1963).
[11]K. S. Pennington and L. H. Lin, Appl. Phys. Lett. 7, 56 (1965).
[12]G. W. Stroke and A. E. Labeyrie, Phys. Lett. 20, 368 (1966).
[13]C. B. Burckhardt, J. Opt. Soc. Am. 56, 1502 (1966).
[14]D. L. Staebler and J. J. Amodei, J. Appl. Phys. 43, 1042 (1972).
[15]Y. Ninomiya, J. Opt. Soc. Am. 63, 1124 (1973).
[16]See, for example, T. K. Gaylord, Opt. Spectra 8, 29 (1974).
[17]P. Phariseau, Proc. Indian Acad. Sci. A 44, 165 (1956).
[18]S. F. Su and T. K. Gaylord, J. Opt. Soc. Am. 65, 59 (1975).
[19]D. Kermisch, J. Opt. Soc. Am. 61, 1202 (1971).
[20]D. Kermisch, J. Opt. Soc. Am. 59, 1409 (1969).
[21]N. Uchida, J. Opt. Soc. Am. 63, 280 (1972).
[22]T. K. Gaylord, T. A. Rabson, and F. K. Tittel, Appl. Phys. Lett. 20, 47 (1972).
[23]F. Micheron and G. Bismuth, Digest of Technical Papers, 1972 IEEE International Solid-State Circuits Conference, p. 104 (unpublished).
[24]W. Phillips, J. J. Amodei, and D. L. Staebler, RCA Rev. 33, 95 (1972).

[25]L.H. Lin, Proc. IEEE 57, 252 (1969).
[26]F.S. Chen, J.T. LaMacchia, and D.B. Fraser, Appl. Phys. Lett. 13, 223 (1968).
[27]J.J. Amodei, W. Phillips, and D.L. Staebler, Appl. Opt. 11, 390 (1972).
[28]A. Ishida, O. Mikami, S. Miyazawa, and M. Sumi. Appl. Phys. Lett. 21, 192 (1972).
[29]R.W. Damon, D.H. McMahon, and J.B. Thaxter, Electro-Opt. Syst. Des. 2, 68 (1970).
[30]F. Micheron and G. Bismuth, Appl. Phys. Lett. 23, 71 (1973).
[31]T.A. Shankoff, Appl. Opt. 7, 2101 (1968).
[32]W. Phillips and D.L. Staebler, J. Electron. Mater. 3, 601 (1974).
[33]D.L. Staebler and W. Phillips, Appl. Opt. 13, 788 (1974).
[34]J.P. Huignard, J.P. Herriau, and F. Micheron, Appl. Phys. Lett. 26. 256 (1975).
[35]D.L. Staebler, W.J. Burke, W. Phillips, and J.J. Amodei, Appl. Phys. Lett. 26, 182 (1975).
[36]J.J. Amodei, D.L. Staebler, and A.W. Stephens, Appl. Phys. Lett. 18, 507 (1971).
[37]F. Micheron and G. Bismuth, Digest of Technical Papers, Optical Storage of Digital Data, MB3-1, 1973 (unpublished).
[38]T.K. Gaylord, T.A. Rabson, F.K. Tittel, and C.R. Quick, Appl. Opt. 12, 414 (1973).
[39]R.L. Townsend and J.T. LaMacchia, J. Appl. Phys. 41, 5188 (1970).
[40]J.J. Amodei and D.L. Staebler, Appl. Phys. Lett. 18, 540 (1971).
[41]D.L. Staebler and J.J. Amodei, Ferroelectrics 3, 107 (1972).
[42]T.K. Gaylord, T.A. Rabson, F.K. Tittel, and C.R. Quick, J. Appl. Phys. 44, 896 (1973).
[43]E.N. Leith, A. Kozma, J. Upatnieks, J. Marks, and N. Massey, Appl. Opt. 5, 1303 (1966).
[44]K. Biedermann, S.I. Ragnarsson, and P. Komlos, Opt. Commun. 6, 205 (1972).
[45]V.V. Aristov and V.Sh. Shekhtman, Sov. Phys. Usp. 14, 263 (1971).
[46]R.G. Zech, Ph.D. thesis (University of Michigan, 1974) (unpublished).
[47]D.R. Bosomworth and H.J. Gerritsen, Appl. Opt. 7, 95 (1968).
[48]T.K. Gaylord and F.K. Tittel, J. Appl. Phys. 44, 4771 (1973).

IV. NEW MASS DATA STORAGE ARCHITECTURES

The development of a high capacity computer memory with a multi-port simultaneous access capability may require new computer architectures for efficient computation. The implications of this are discussed in Reference [7], which is reproduced on the following pages of this report.

THE POTENTIAL OF MULTI-PORT OPTICAL MEMORIES IN DIGITAL COMPUTING

C. O. Alford and T. K. Gaylord
School of Electrical Engineering
Georgia Institute of Technology
Atlanta, Georgia 30332

Summary

A high-capacity memory with a relatively high data transfer rate and multi-port simultaneous access capability may serve as the basis for new computer architectures. The implementation of a multi-port optical memory is discussed. Several computer structures are presented that might profitably use such a memory. These structures include (1) a simultaneous record access system, (2) a simultaneously shared memory computer system, and (3) a parallel digital processing structure.

Introduction

It is widely recognized that the characteristics of optical memories are different from those of conventional computer memories. Thus, they may play roles that are different from the roles played by existing magnetic and semiconductor memories. One potential capability of optical holographic memories as suggested by Rajchman [1] is the replacement of a large fraction of the conventional computer memory hierarchy. In this situation a series of slow and large, and fast and small memory devices would be replaced by a single optical memory unit. This may be possible due to the potential coexistence of both high capacity and fast access times in an optical memory--two features that do not exist together in conventional memories.

In addition, there are other ways that optical memories may be distinctly different from conventional memories. One of these is the multi-port capability--the capability of stored data in the memory to be accessed simultaneously by multiple users through each of the memory's ports. This is to be contrasted with space multiplexed (interleaved) and time multiplexed conventional memories which are sometimes represented as being "multi-port." However, a true multi-port memory allows simultaneous access to its data through each memory port.

Multi-Port Optical Memories

Multi-port optical memories could be of a variety of designs. A possible example of a multi-port holographic memory is shown in Fig. 1. In this diagram, the recording medium is being used as a two dimensional store rather than a three dimensional store [2]. There is one page of binary data stored in holographic form at each x-y location of the recording medium. This memory is basically the same as a conventional optical holographic memory [3] except that 1) there are three extra beam deflectors and 2) there is one read-out detector matrix for each memory port. The extra beam deflectors are of key importance in this memory system. The first reference/read-out beam deflector produces N beams deflected by varying amounts in the y direction. The second reference beam deflector is a one dimensional array of deflectors to produce deflection of the reference beams by varying amounts in the x direction. Finally, the readout deflector array is a two dimensional array of deflectors directly behind the recording medium to steer the reconstructed data beam to the appropriate memory port [4]. Notice that this memory configuration uses a single page composer for writing in data at all x-y hologram locations in the recording medium.

The complexity of a multi-port optical memory is thus greater than that of a single port optical memory. However, the cost of additional memory ports beyond the second port would be relatively small. For each additional port, the primary additions would be another read-out detector matrix and an increase in laser power. There would be one reference/read-out beam for each of the N ports. With additional ports, the basic object beam and reference/read-out beam configurations as illustrated in Fig. 1 would not be changed. An upper limit on the number of ports would obviously be imposed by the amount of usable space available behind the inverse Fourier transform lens.

Simultaneous Record Access System

One of the prime purposes of a high-capacity optical memory is to store vast quantities of records or information such as libraries, insurance data, medical data, seismic data, criminal data, defense data, tax information, patent records, telephone numbers, stock market information, etc. Users of such a storage bank would need to have access to page information. Further, multiple user capability is required to make such a system cost effective. A possible structure for this system is shown in Fig. 2.

Data is stored in page format in the multi-port optical memory. Access to any page is via a terminal (CRT type) through one of the memory access ports. The data requirements of each terminal are, in some applications, low enough to have one memory port support several terminals through a multiplexer. Since a single page access may require on the order of 1 μsec and since each human user would take on the order of 1 minute to scan a page and reach a decision on the next access, a single port operating through a multiplexer could theoretically support 10^6 terminals. However, maximum data rates between the port and the terminal will reduce this number to the order of probably 100. Thus ten ports could support 1000 users and this could be extended to more users by increasing the data rates on the external circuitry.

Trade-offs are between port speed, multiplexer speed and numbers of ports. The most effective system would match the total number of users at one port to an economical multiplexer such that the average access time for any user is reasonable (approx. 1 min.). This access time divided by the number of users per port fixes the multiplexer speed and memory access time per page. If a slower memory access time can result in a less expensive memory or if this can be traded for additional memory ports at the same expense, these would make desirable trade-offs.

The normal mode of page read-out is a binary pattern of a discrete number of bits. It is conceivable, however, that certain information, such as pictures and figures, would be read out of the optical

memory in a non-encoded format. The transfer of this type of information to a readable display for multiple users, presents a number of new design problems and trade-offs.

The user terminals are normally used in the read-only mode and are not allowed to perform write operations to memory. Writing would be done by an input terminal through a separate memory port. Since this is also a low speed operation, this port could be multiplexed to other terminals for further read-only usage.

Simultaneously Shared Memory Computer System

The record access application did not require any transformations on the data accessed by the user. If such transformations are necessary, arithmetic logic units must be added to the architecture. One such structure is shown in Fig. 3. The system is essentially the same as most current time-sharing structures. Several users are allowed access to a processing unit. Primary memory is allocated and user programs are executed independently of the multi-port secondary memory, if possible. Calls to special application programs and large blocks of data are achieved by swapping that data in and out from the multi-port memory.

The secondary memory serves as a backing store mass memory device. Its multi-port structure, however, makes it functionally equivalent to several disk drives and its transfer rate makes it superior to the parallel operation of disk units. The possibility exists of placing most of the operating system in the optical memory and decreasing the size of the primary memory units for each central processor unit (CPU).

Some of the parameters needed to characterize such a system are number of bits per page, number of pages, number of ports, access time, primary memory size, write protection scheme, and division of the operating system between the primary memory and the multi-port memory. Trade-offs exist between these parameters and it would appear that if primary memory can be effectively reduced by utilizing the optical memory, a more cost efficient time sharing system would result. Since swapping of information between memories is a common problem in time-sharing systems, the potential access ease and speed of moving pages in and out of the optical memory would be a definite improvement. Other trade-offs exist between the number of ports and number of users and the port speed necessary for a single CPU.

Parallel Digital Processing

There are many scientific problems which require an enormous number of computations. One approach to this problem has been a multi-processor parallel computation technique. Essentially all processors are dedicated to solving one step of the problem. The results are then transfered to the appropriate processor that is dedicated to solving the next step of the problem. Likewise, the first processor also receives new input data and the step-wise computation continues. Problems arise from synchronization and system reliability when the parallelism is carried as far as that in Illiac IV. While no structure is being proposed which would duplicate the Illiac IV performance, it is believed the multi-port memory with a minicomputer multiprocessor structure could give surprising performance.

A possible structure based on a single bus (Unibus) architecture similar to the Lockheed Sue computer is given in Fig. 4. Each minicomputer (module) contains its own processor, data source, and instruction memory. The Unibus allows this module to function as a separate computer independent of the other processors and the multi-port memory. Each module is connected to the multi-port memory through a port and a page memory buffer. This buffer is then tied to the Unibus for transfers to the processor and other memory units. Transfers between modules are made on an outer bus connecting each module.

An alternate configuration which places control of all processors under the direction of one control computer (CPU) is shown in Fig. 5. Instructions are kept in the optical memory and fetched by the control computer. These instructions are sent along the outer bus to selected CPU modules. Modules can then execute similar instructions or different instructions according to the demands of the control computer. All data on which the modules will operate moves through the ports, page buffers, and data memories to be transformed by the processors.

Some of the characteristic parameters of these systems are number of bits per page, number of pages, number of ports, page transfer rates, bus transfer rates, and types of synchronization signals. Trade-offs exist between computational speed of the processors, number of ports and access time. It would seem that the control computer of Fig. 5 would have to be considerably faster than the other processors and possibly the port under its control, port 0, would have to have a higher speed than other ports.

Acknowledgements

This work was supported in part by the National Science Foundation under Grant No. GK-37453 and by the National Aeronautics and Space Administration under Contract No. NAS8-30246.

References

1. J. A. Rajchman, "Promise of Optical Memories," J. Appl. Phys., vol. 41, pp. 1376-1383, March 1, 1970.
2. e.g. L. d'Auria, J. P. Huignard, C. Siezak, and E. Spitz, "Experimental Holographic Read-Write Memory using 3-D Storage," Appl. Optics, vol. 13, pp. 808-818, April 1974.
3. e.g. W. C. Stewart, R. S. Merzrich, L. S. Cosentino, E. M. Nagle, F. S. Wendt, and R. D. Lohman, "An Experimental Read-Write Holographic Memory," RCA Review, vol. 34, pp. 3-44, March 1973.
4. A possible technology for this is described in Y. Ninomiya, "High s/n-Ratio Electrooptic Prism-Array Light Deflectors," IEEE J. Quantum Electron, vol. QE-10, no. 3, pp. 358-362, March 1974.

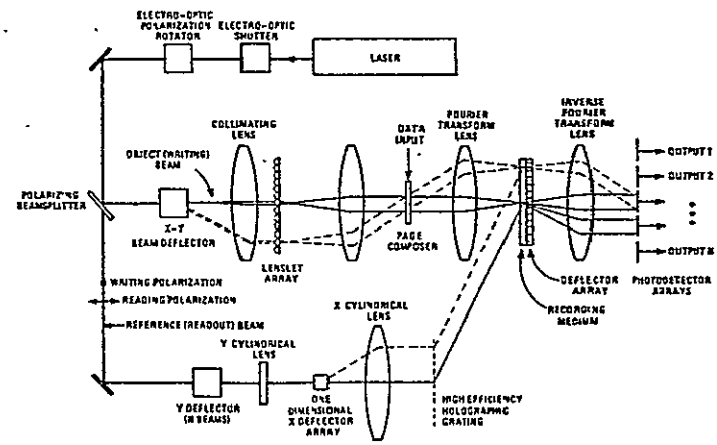

Fig. 1. A multi-port optical memory.

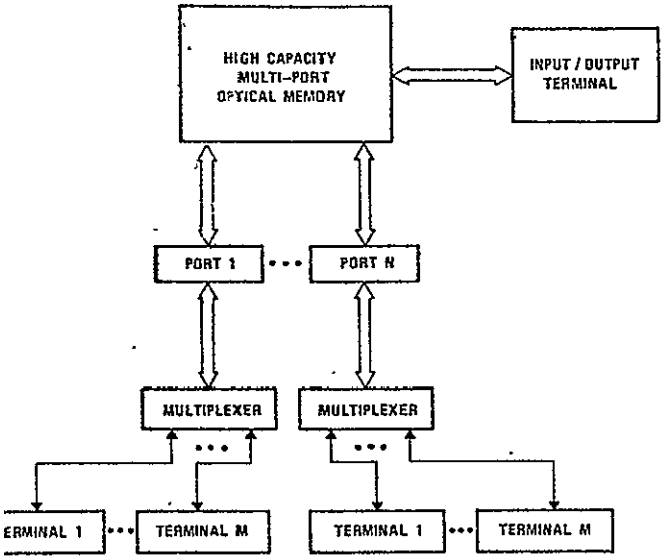

Fig. 2. Computer architecture for a record access system.

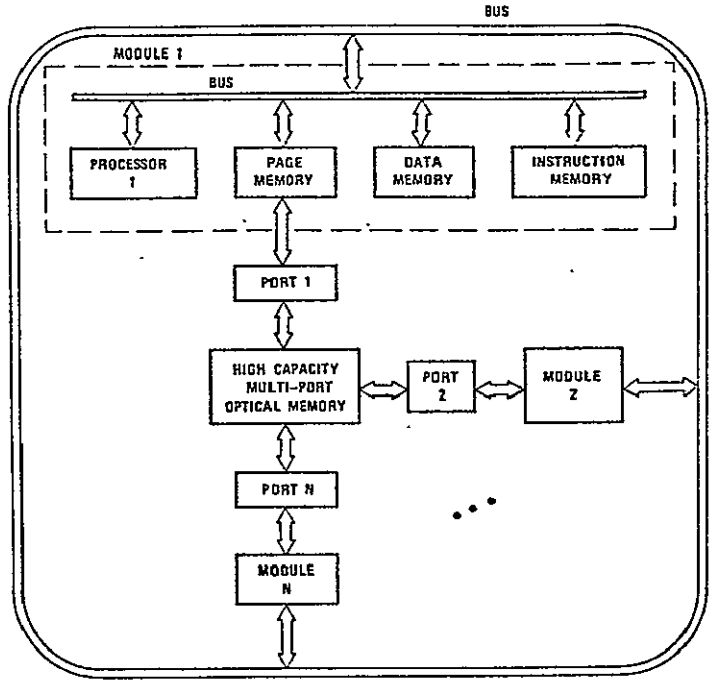

Fig. 4. Computer structure for parallel processing.

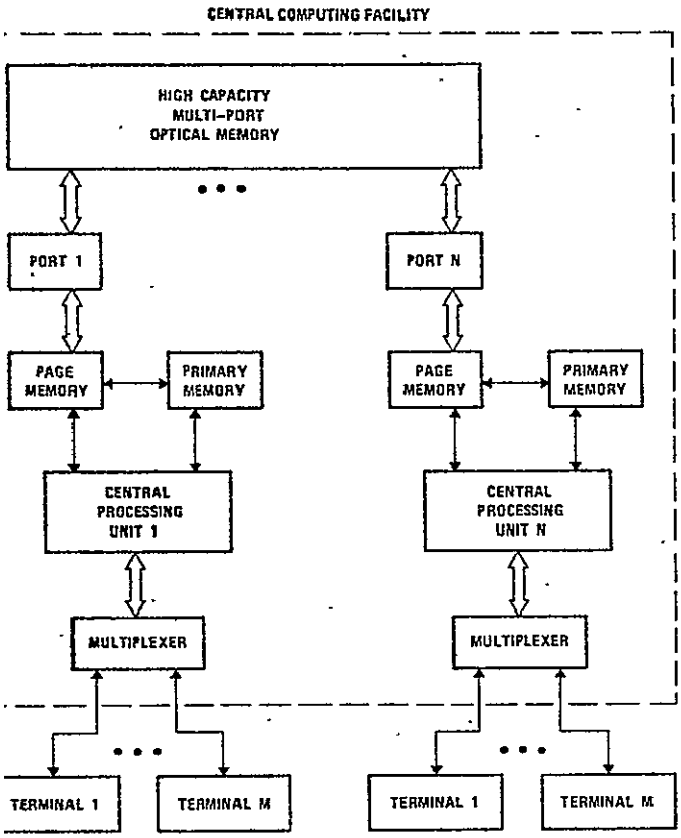

Fig. 3. Simultaneously shared memory computer system.

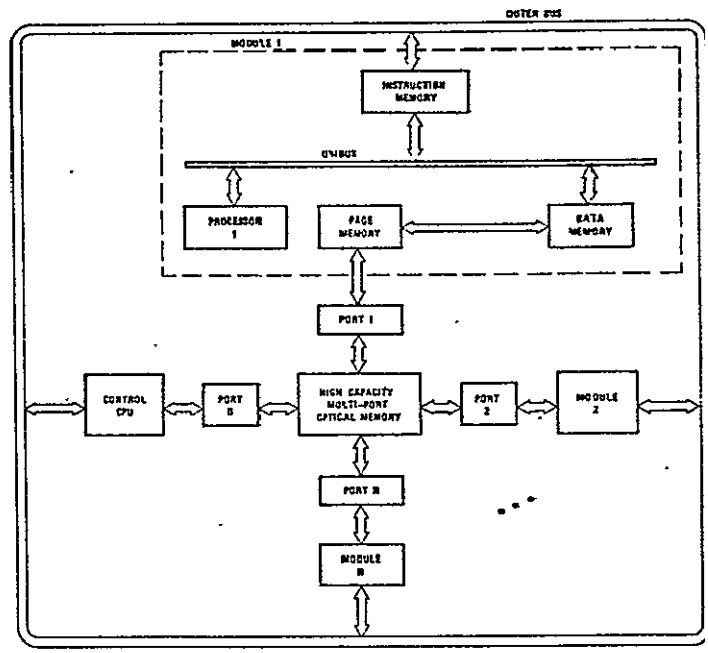

Fig. 5. Synchronized parallel processing computer structure.

V. MULTIPLE RECORDING OF HOLOGRAMS

This section of the report details experimental efforts to store multiple holograms at a single location in a crystal of lithium niobate. Seven holograms of different data masks with an angular separation of 2.97 milliradians were successfully written at a single location, and reconstructed, and ten holograms of the same data mask with an angular separation of 4.75 milliradians were successfully written at a second location and reconstructed.

MULTIPLE RECORDING OF HOLOGRAMS

J. E. Weaver and W. R. Callen

APPARATUS

The experimental configuration depicted in Figure 1 was used in all experiments described in this section of the report. The entire experimental arrangement is mounted on an air suspension stable table. The laser used to perform the multiple recording is a 5mW Spectra Physics HeNe gas laser. The crystal was mounted in a modified commercial lens positioner. The modifications included an x-y stage that allowed crystal movement only, in order to vary the location of the interference pattern on the crystal. The retransform lens was rigidly mounted to the entire assembly, which was capable of xyz displacement and capable of deflection in the ϕ and θ (horizontal and vertical) planes. This crystal mount allowed the retransform lens to remain fixed relative to the crystal. By moving the crystal-retransform lens assembly and keeping the reference (R) beam fixed, it was possible to duplicate optically the effect of motion of the R beam relative to a stationary crystal and transform lens assembly. The advantage of this approach is that a stationary R beam may be easily spatially filtered and controlled in diameter. The wavefront does not undergo the distortion produced by an actual deflector. Although in any working memory system, beam deflectors will probably be used, the arrangement used here enables one to study the multiple storage effects in isolation from beam deflection considerations.

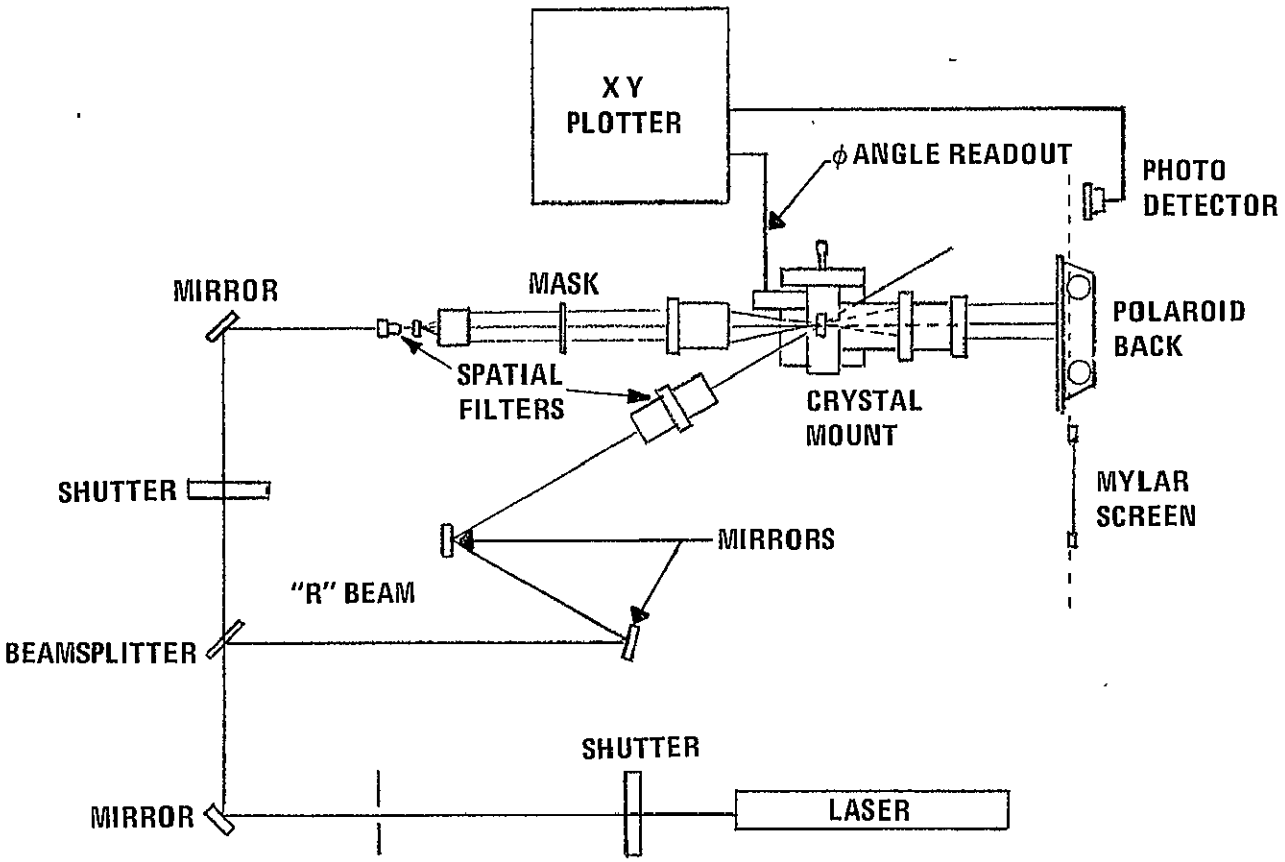

FIGURE 1. Experimental configuration for study of multiple hologram recording.

The transform optics employed were two f/3.5, 200 mm diameter Cooke triplets. The signal beam is formed by passing the laser beam, after spatial filtering and collimating, through a square aperture framing a transparency. The reference beam is also spatially filtered and collimated.

The effective waist diameter of the transformed signal (S) beam as a function of distance along the optical axis (Z direction) is shown by the curve indicated by (0) data points in Figure 2. This waist is defined by visual determination, as opposed to the $1/e^2$ definition employed for Gaussian beams. The width of the central spot of the transform is indicated by (x) data points in Figure 2. The effective diameter of the collimated and spatially filtered reference beam can be determined from Figure 3, which shows a plot of transmitted power versus position of a knife edge that is movable in the y direction.

The region of the holographic grating occurs where both the signal and the reference beams are of approximately equal intensity. This region may be approximated by the first few orders of the one dimensional Fourier transform of the checkerboard-type mask, as shown in Figure 4.

Since the pattern of the mask is similar in both x and y directions, we can characterize it by considering a one-dimensional transmissivity function:

$$t(x) = \text{rect}\left(\frac{x}{16a}\right)\left[\text{comb}\left(\frac{x}{2a}\right) * \text{rect}\left(\frac{x}{a}\right)\right], \qquad (1)$$

using the notation of reference [1]. The actual data mask had 16 squares in each dimension.

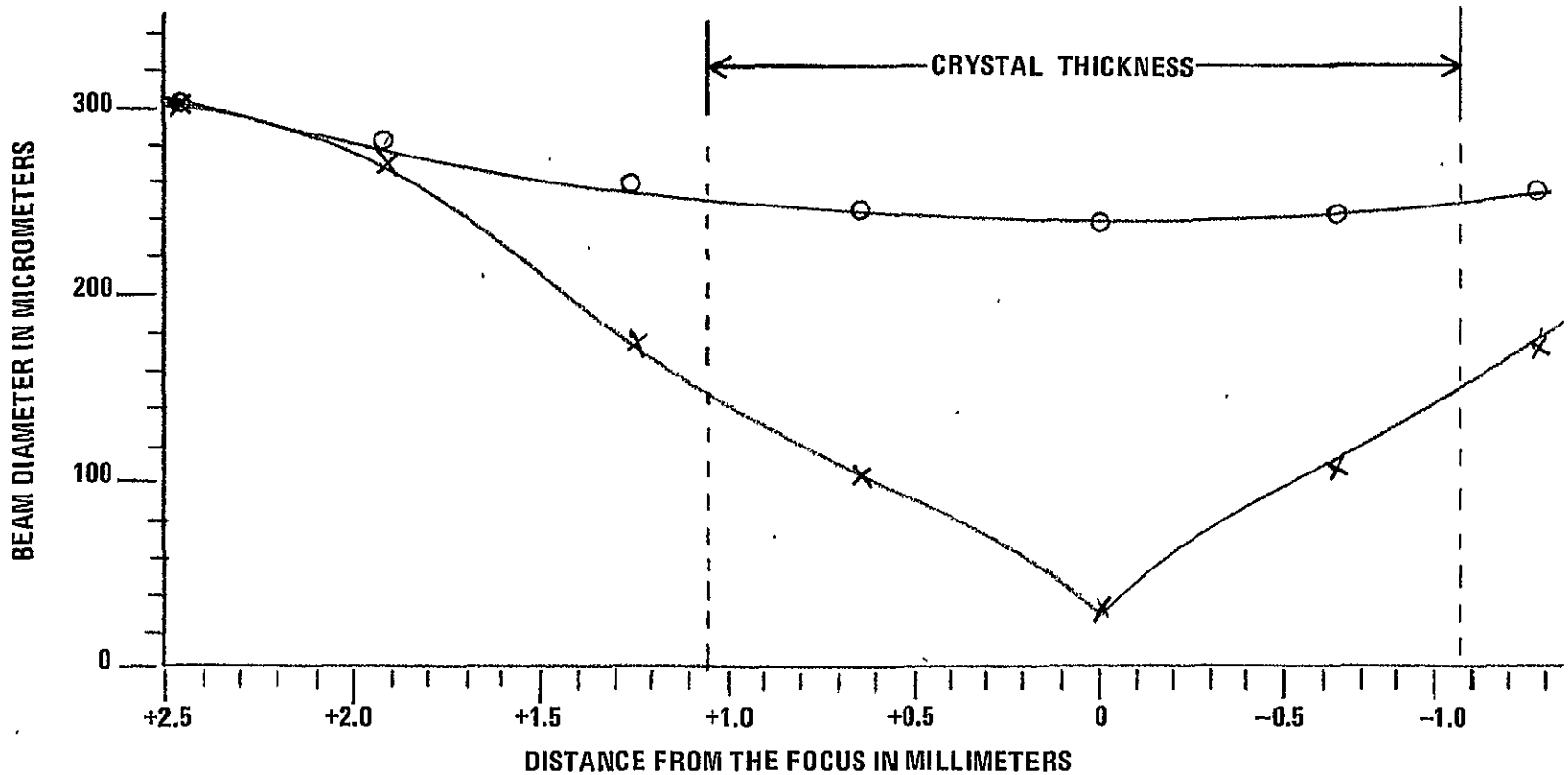

FIGURE 2. Signal ("S") beam diameter as a function of position along the optical axis.

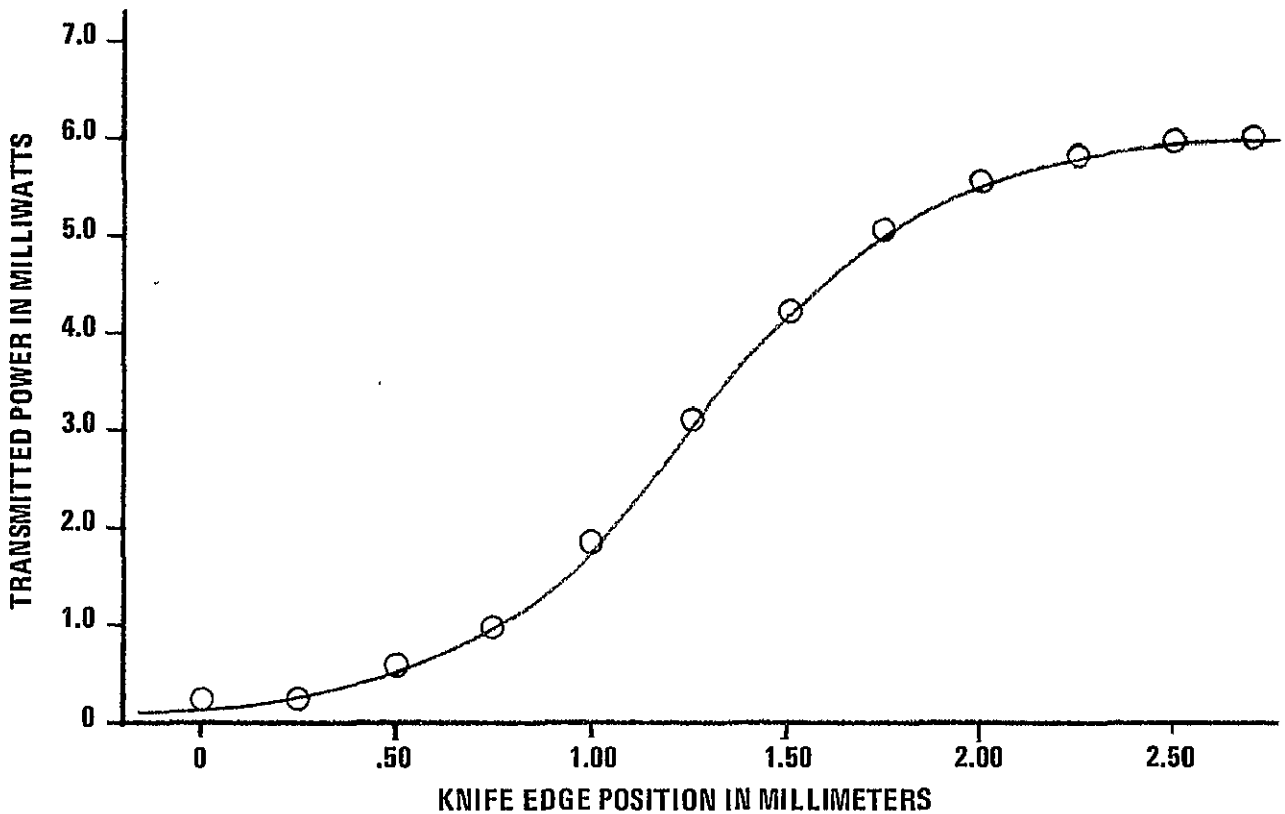

FIGURE 3. Reference ("R") beam diameter determination.

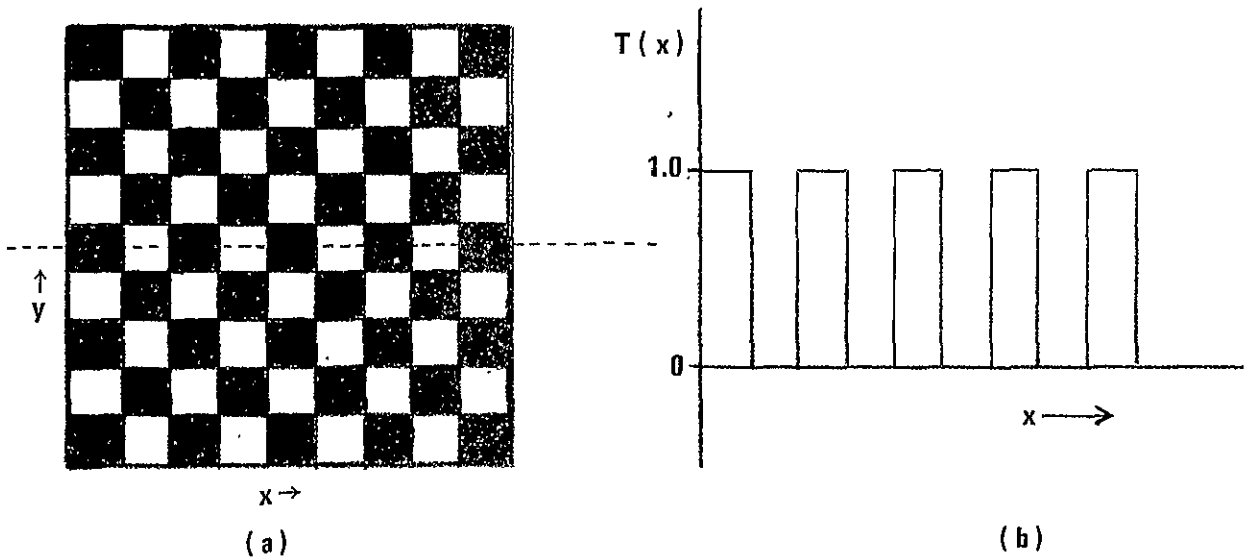

FIGURE 4. (a) Checkerboard mask used to produce signal beam pattern
(b) One-dimensional transform of checkerboard mask (at one value of y)

The transform of Equation (1) is

$$\{t(x)\} = 32a^3 \text{sinc}(16af_x) * [\text{comb}(2af_x)\text{sinc}(af_x)] \qquad (2)$$

where $f_x = x_2/\lambda f_\ell$, with λ as the wavelength of light and f_ℓ the focal length of the transform lens. The transform describes the electric field distribution in a line described by the spatial variable x_2 and positioned one focal length from the transform lens on the opposite side from the data mask. For our experiment, $a=1.06\text{x}10^{-3}$m, $f_\ell=2\text{x}10^{-1}$m, and $\lambda=6.33\text{x}10^{-7}$m. For a perfect thin lens, the power in the first n orders is confined to a circular region that is $(2n+1)\Delta$ in diameter, where Δ is the distance in the (x_2,y_2) plane between any two adjacent orders. For the transform defined by equations (1) and (2), we have

$$\Delta = \frac{\lambda f_\ell}{2a} = 59.7 \text{ μm}.$$

The region of the first three orders exists within a region of diameter [2(2)+1][59.7] μm = 298.5 μm. Therefore, we may assume that the hologram exists within a cylinder 300 μm in diameter, which is substantiated by Figure 2.

EXPERIMENTAL PROCEDURE

The crystal used for all experiments was an iron-doped lithium niobate ($LiNbO_3$) crystal (.1 mole per cent F_e in melt). The crystal was 2.12 mm thick, with an average absorption coefficient of 3.15 cm^{-1} and exhibited extremely high light sensitivity.

Two experiments were conducted to illustrate multiple recording of images in $LiNbO_3$. In the first experiment, seven different high contrast images were written at one location in the crystal. The

reconstructed images and the angular separations were recorded. In the second experiment, diffraction efficiency was measured as a function of angle for the reconstruction of the same mask recorded ten times at the same location. The total diffracted power and angular position of the R beam was recorded.

First Experiment. The S beam was attenuated by approximately 30 db and positioned on the crystal. A photograph of the image of the S beam only was made, shown in Figure 5a. The neutral density filter was removed, and the ratio of power of the R beam to that of the S beam was adjusted to fifty; the total beam power was 3.5×10^{-5} watts. A ten second exposure was made with both beams. The reconstruction of the R beam was photographed (Figure 5b). The crystal was displaced in the ϕ direction as the attenuated reconstruction was observed. When the reconstruction was extinct, the change in ϕ was calculated to be .17 degrees (2.97 milliradians). Without further change in crystal orientation, the mask was changed, and a second exposure of ten seconds was made with both S and R beams. The crystal was displaced again in the ϕ direction by .17 degrees, the mask was changed, and another ten second exposure was made with both beams. This procedure of crystal displacement, mask changing, and dual beam exposure was repeated until seven holograms of different masks were written at the same location. Using the R beam only, the reconstructions of all seven holograms were photographed (Figures 5b through 5h).

The results illustrate that the high constrast masks were reconstructed. The noise present in the reconstruction may be divided into three sources: 1) spatial noise present in the optical system;

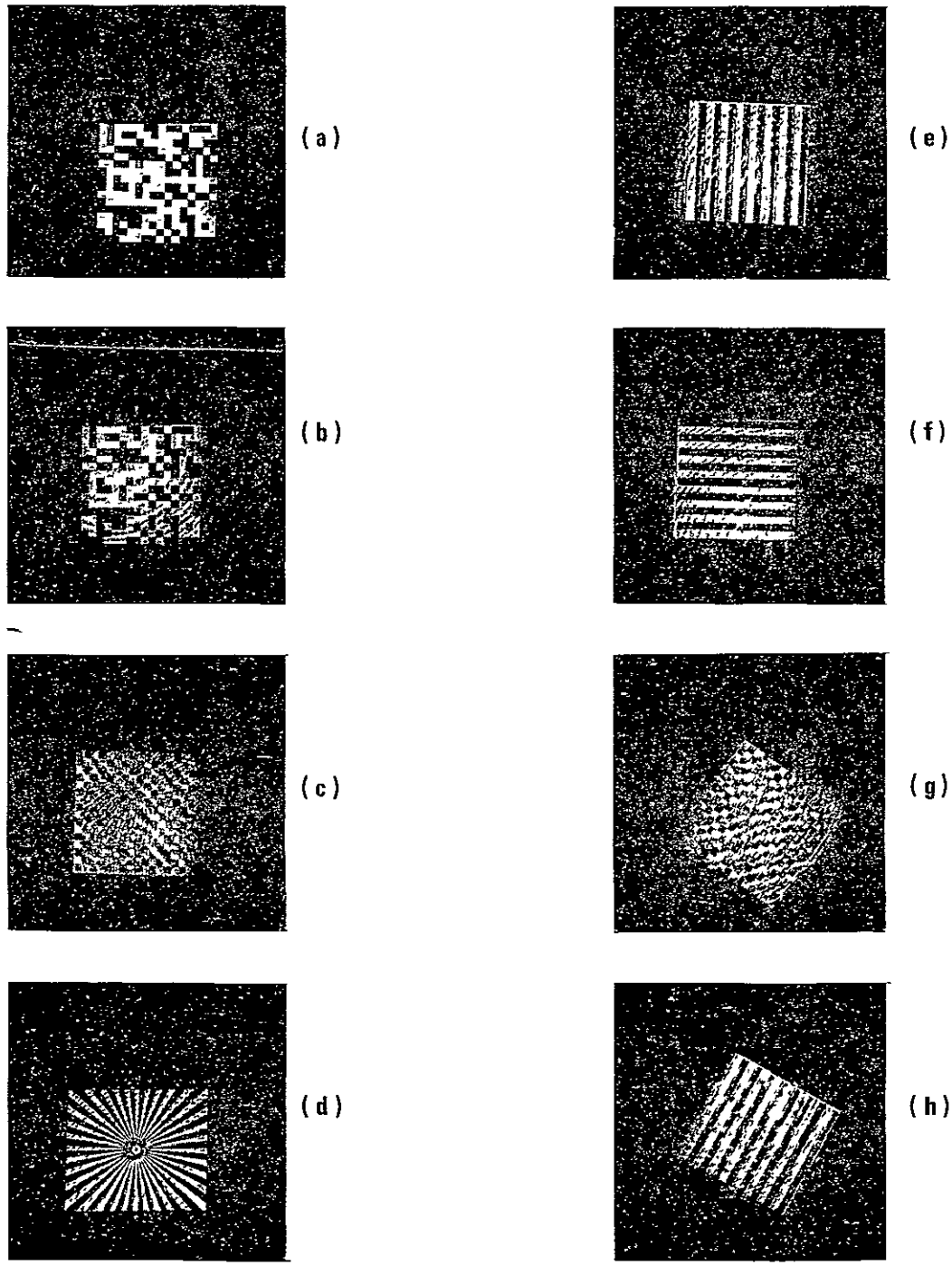

FIGURE 5. Photographs of (a) signal beams, (b)-(h) reconstruction of seven holograms.

2) scattering and aberrations present in the recording medium, and 3) cross-talk from adjacent holograms.

Optical system noise produces the concentric ring pattern that may be seen in all images. This pattern remains fixed as the crystal is rotated, which indicates that this pattern is not produced by the recording medium. This ring pattern is also observed using the S beam only, which indicates that holographic reconstruction noise and aberrations are not contributing.

Noise due to scattering and aberrations of the recording medium are exhibited as 1) blurring or fringes around the high contrast-high spatial frequency edges; 2) dark regions in the center of extended light areas and vice-versa; and 3) speckle noise distributed through the circular region corresponding to the clear aperture of the lens.

Cross-talk due to adjacent holograms is not inherent in the reading operation, but is due to poor repeatability in the Φ positioning operation.

Second Experiment. Using the same experimental arrangement as in the first experiment, but without changing the mask, ten holograms were written. The angular separation between holograms was 4.75 milliradians (.272°). The total diffracted power and diffraction efficiency for each of the ten holograms is shown in Table 1. A plot of the diffracted power versus angle is shown in Figure 6. The approximate diffraction efficiency based on an estimate of hologram size is shown on the right side of Figure 6. The typical base width of each reconstruction is 3.8×10^{-3} radians and the half power width is 1.9×10^{-3}

TABLE I. Multiple Hologram Data (Second Experiment)

Hologram (in order of writing)	Total Diffracted Power (μ watts)	Diffraction Efficiency (%)
1	1.45	3.4
2	3.75	8.6
3	1.46	3.4
4	2.44	5.6
5	2.98	6.9
6	3.27	7.6
7	2.53	5.8
8	3.78	8.7
9	2.16	5.0
10	2.88	6.6

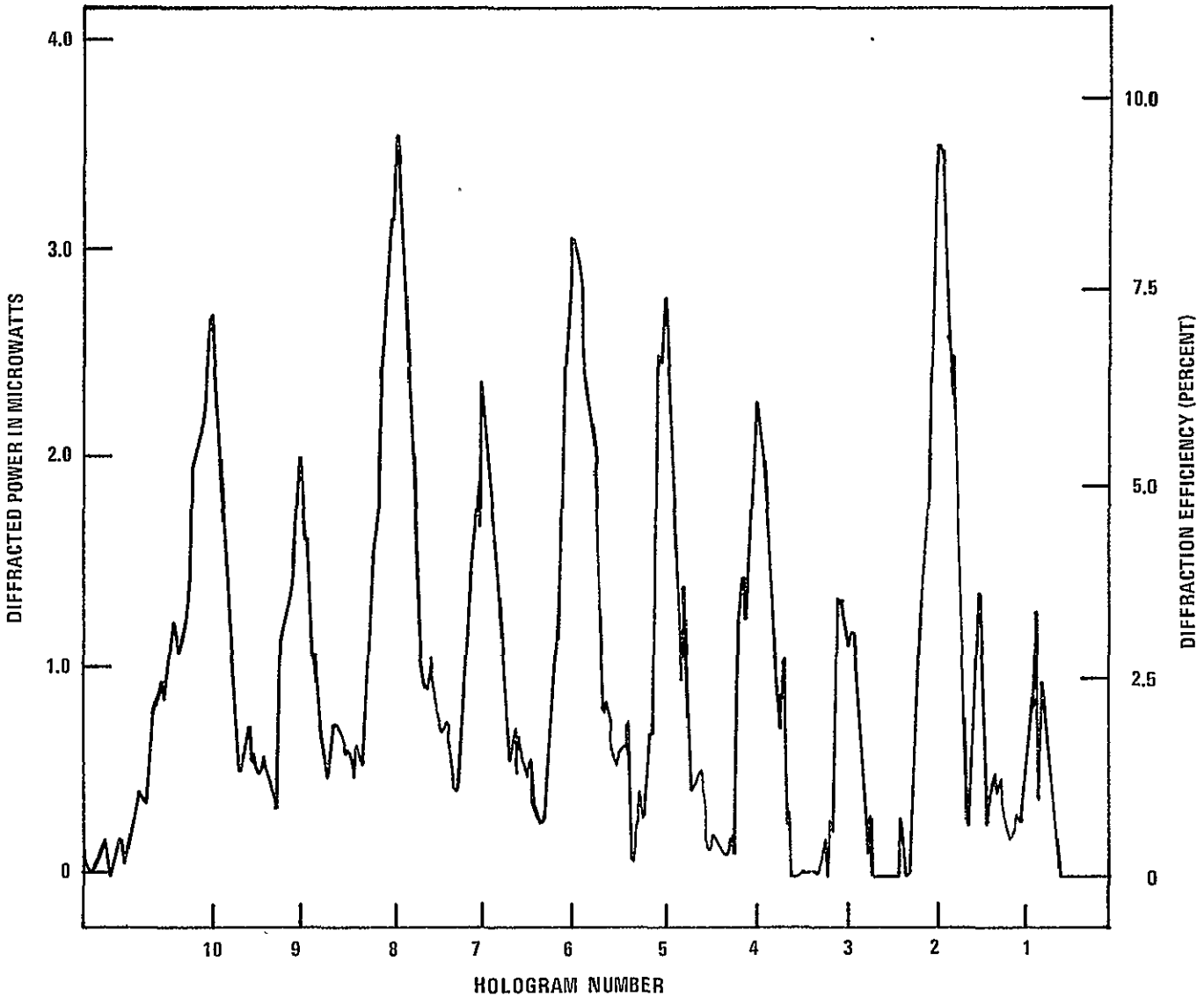

FIGURE 6. Plot of diffracted power versus angle.

radians. The first hologram (extreme right of Figure 6) is noisy and reduced in diffraction efficiency, because this hologram was exposed longer than were the other holograms while the quality of the reconstuction was examined visually with the full power R beam.

FUTURE WORK

Future work in this area will be to reduce the spatial noise in the recording system, calculate and measure the R beam positioning sensitivity, develop an optimum mask for the storing of data, and examine the relationship between the relative strength of object and reference beam and diffraction efficiency.

REFERENCES

[1] J. W. Goodman, Introduction to Fourier Optics, New York: McGraw-Hill, 1968, pp. 9-17.

REFERENCES

[1] J. J. Amodei, "Analysis of transport processes during holographic recording in insulators," RCA Review, vol. 32, pp. 185-199, June 1971.

[2] S. F. Su and T. K. Gaylord, "Unified approach to the formation of phase holograms in ferroelectric crystals," J. Appl. Phys., vol. 46, no. 12, pp. 5208-5213, December 1975.

[3] S. F. Su and T. K. Gaylord, "Determination of physical parameters and processes in hologram formation in ferroelectrics," J. Appl. Phys., vol. 47, no. 6, pp. 2757-2758, June 1976.

[4] S. F. Su and T. K. Gaylord, "Refractive-index profile and physical process determination in thick gratings in electro-optic crystals," Appl. Optics, vol. 15, no. 8, August 1976 (to appear).

[5] C. B. Burckhardt, "Diffraction of a plane wave at a sinusoidally stratified dielectric grating," J. Opt. Soc. Am., vol. 56, pp. 1502-1509, November 1966.

[6] H. Kogelnik, "Coupled-wave theory for thick hologram gratings," Bell Syst. Tech. J., vol. 48, no. 9, pp. 2909-2947, November 1969.

[7] R. Magnusson and T. K. Gaylord, "Use of dynamic theory to describe experimental results from volume holography," J. Appl. Phys., vol. 47, no. 1, pp. 190-199, January 1976.

[8] C. O. Alford and T. K. Gaylord, "The potential of multi-port optical memories in digital computing," Proc. of the International Optical Computing Conference, Washington, D.C., April 1975.